NTNU – Trondheim
Norwegian University of
Science and Technology

Finite Element Simulations of Punch Tests on Ice Rubble with the Modified Cam Clay Model

Comparison of Full Scale and Model Scale Experiments

Hege Lindbjør Nilsen

Civil and Environmental Engineering
Submission date: June 2015
Supervisor: Knut Vilhelm Høyland, BAT
Co-supervisor: Nicolas Serré, Multiconsult

Norwegian University of Science and Technology
Department of Civil and Transport Engineering

Preface

This Master's thesis was written during the spring semester of 2015 as a part of the masters degree in Civil and Environmental Engineering at the Norwegian University of Science and Technology (NTNU). The thesis was written at the Department of Civil and Transport Engineering (BAT), Faculty of Engineering Science and Technology (IVT), in collaboration with Multiconsult Tromsø, department of Arctic and Marine Technology.

The work involved numerical simulations of both model scale and full scale punch tests on ice ridges, aiming to determine the material properties of the ice rubble. The main goal was to figure out how to scale the mechanical properties of artificially produced model scale ice ridges. A great deal of time was spent solving numerical issues connected to explicit analysis - herein trying to improve the energy results and investigating which effect different modelling options had on the output. The analyses were performed with a Coupled Eulerian-Lagrangian formulation, which required a substantial amount of elements, thereby causing time consuming analyses.

I would like to thank my main supervisor, professor Knut Vilhelm Høyland, for providing valuable guidance and for always taking the time to discuss my thesis despite his busy schedule. I would also like to thank my co-supervisor Nicolas Serré at Multiconsult Tromsø, for his help during both the current and the previous semester. There were a number of people involved in the process of solving the numerical issues concerning the energy balance, and I would in particular like to mention PhD candidates Sergey Kulyakhtin, at the Department of Civil and Transport Engineering, and Martin Kristoffersen, at the Department of Structural Engineering. Last, but not least, I would like to thank my boyfriend Jonas Stene Pettersen for proofreading the report and for endless discussions and patience despite his limited knowledge in the field.

This thesis is written based on the the assumption that the reader has some knowledge about finite element calculations, and even though the material model is quite thoroughly explained, some basic knowledge about elastic-plastic materials and geotechnical properties is anticipated.

Trondheim, 2015-06-10

Hege Lindbjør Nilsen

Summary

Ice ridges are features created by the relative motion between ice sheets, and appear as a pile up of broken ice or ice blocks both above (sail) and below the water surface (keel). First-year ice ridges are important in the design of offshore and marine structures, but the knowledge about the ice ridge properties are still limited. Model scale experiments on artificially produced ice ridges have been developed, leaving the question of how to scale the properties correctly.

This thesis concerns the scaling of the properties of the unconsolidated layer of the keel (the ice rubble) from model scale to full scale, as a part of the determination of ice ridge properties for design. Two types of punch tests have been simulated numerically in order to study the difference between the required material parameters:

1. Four full scale punch tests performed in the Gulf of Bothnia in 1999
2. Two model scale punch tests performed at the Hamburg Ship Model Basin (HSVA) in 2001

The punch tests involve loading the ice ridge with a loading plate while measuring the resistance from the ridge. The experiments were modelled in the Finite Element software Abaqus, version 6.12, using explicit analysis. Both cases were modelled using the Coupled Eulerian-Lagrangian (CEL) approach, which copes with the challenge of large displacements of the ice rubble as well as the interface between the puncher and the ridge. The ice rubble was described using the Modified cam clay material model. This material model was originally developed for clays and has been used due to its relatively simple formulation and because it allows for volumetric changes.

The numerical simulations successfully managed to fit the experimental results until the maximum force was reached. After the peak force, the ice ridges in the experiments failed in shear. The global failure caused a large load drop which was not captured in the numerical simulations since the Modified cam clay model does not include a failure criterion.

The depth measurements of the keel turned out to be vital for the numerical determination of the keel resistance, underlining the importance of proper field measurements. The loading of the full scale ice ridges was more complex than in the model scale tests, and a more advanced numerical model is probably necessary to properly simulate the entire time history.

The material parameters which influenced the numerical results the most were the stress ratio M and the initial pressure p_0. The stress ratio was about the same for model scale and full scale simulations (1.8-1.85), which is expected since the parameter is dimensionless and dependent upon the critical friction angle. The initial pressure was much larger for the full scale ice ridges, leaving a scale factor (p_0^{FS}/p_0^{MS}) of around 20-40. On the contrary, the length scaling between the two cases were in the order of 10, meaning that the model scale ice ridges are much weaker than the full scale ridges. The large initial pressure required in the full scale simulations resulted in smaller plastic strains than what was the case for model scale.

Sammendrag

En skrugard er en isformasjon som oppstår på grunn av den relative bevegelsen mellom isdekker, og fremstår som en oppbygging av knust is eller isblokker både over (seil) og under vannflaten (kjøl). Førsteårs skrugarder er viktige for design av offshore og marine konstruksjoner, men kunnskapen om materialparametrene er fortsatt begrenset. Modellskala eksperimenter på kunstig framstilte skrugarder har blitt utviklet, men spørsmålet er fortsatt hvordan man skal skalere egenskapene riktig.

Denne oppgaven omhandler skalering av materialegenskapene til det *ukonsoliderte* laget av kjølen fra modellskala til fullskala, som et ledd i bestemmelsen av egenskaper for å kunne regne iskrefter. To typer punchtester har blitt simulert numerisk for å studere forskjellen mellom materialegenskapene:

1. Fire fullskala punchtester utført i Bottenvika i 1999
2. To modellskala punchtester utført i skipsmodelltanken i Hamburg (HSVA) i 2001

Punchtestene går ut på å laste skrugarden ved hjelp av en lastplate samtidig som motstanden fra skrugarden måles. Eksperimentene ble modellert i elementmetodeprogrammet Abaqus, versjon 6.12, ved bruk av eksplisitte analyser. Begge tilfellene ble modellert med en koblet Euler-Lagrange formulering (CEL), som kan takle store forskyvninger samt å definere grenseflaten mellom lastplaten og skrugarden. Det ukonsoliderte laget av skrugarden ble beskrevet med materialmodellen "Modfied Cam Clay". Denne materialmodellen ble originalt utviklet for leire, og har blitt brukt i denne oppgaven på grunn av den relativt enkle formuleringen og fordi den tillater volumforandringer i materialet.

De numeriske simuleringene klarte å etterligne de eksperimentelle resultatene fram til makskraft ble nådd. Etter å ha nådd makskraft går skrugardene i eksperimentene til brudd i skjær. Det globale bruddet forårsaker et stort lastfall som ikke er oppnådd i simuleringene på grunn av at Modified Cam Clay mangler et bruddkriterium.

Dybdemålingene av kjølen viste seg å være viktig for de numeriske beregningene av kjølmotstanden, noe som understreker viktigheten av skikkelige feltmålinger. Pålastningssystemet for de fullskala testene var mer kompleks enn for modellskala, og en mer avansert numerisk modell er antakeligvis nødvendig for å kunne simulere hele tidsintervallet på en nøyaktig nok måte.

Materialparametrene som påvirket de numeriske resultatene mest var spenningsforholdet M og initielt trykk p_0. Spenningsforholdet var omtrent det samme for modellskala og fullskala simuleringer (1.8-1.85), noe som var forventet i og med at parameteren er dimensjonsløs og avhengig av den kritiske friksjonsvinkelen. Det initielle trykket var mye større for fullskala skrugarder, og ga en skaleringsfaktor (p_0^{FS}/p_0^{MS}) på rundt 20-40. Lengdeskaleringen var derimot i størrelsesorden 10, og tyder på at modellskala skrugarder er mye svakere enn fullskala skrugarder. Det store initielle trykket for simuleringene i fullskala resulterte i mindre plastiske tøyninger enn hva som var tilfellet i modellskala.

Contents

1 Introduction

First-year ice ridges are one of the main concerns in offshore engineering. Ice ridges appear as a pile-up of broken ice or ice blocks, both above and below the water line. Because of the large volume of ice located beneath the water surface, denoted the keel, they can exert large forces on offshore structures and contribute to an extensive scouring of subsea structures. Ridges are often found in the zone between land fast ice and drift ice, or partially grounded near shore where they can become several kilometers wide. Ridges or rubble piles may also accumulate in front of larger marine structures such as lighthouses and bridge piers (Heinonen, 2004).

Although the importance of ice ridges is well-known, the knowledge about their properties is limited. This is both due to limited research in the area as well as less developed methods for investigation, giving less reliable results. Properties of ice ridges vary both in time and space, complicating the determination of its material behaviour and making investigations essential. In-situ testing is subject to difficult conditions and limited accessibility. Model scale testing has proven to be valuable, but a main obstacle is the question of how to scale the properties retrieved in model scale to full scale.

A clear connection is still to be found between the properties of the ridge and the load it exerts. This raises the need for numerical simulation. Numerical methods such as the Finite Element Method can be used to:

- Find and develop material models that can describe the behaviour of ice in the best possible way
- Simulate experiments to find material parameters
- Simulate and estimate the action of sea ice and ice ridges on structures

The primary aim is to find a way to estimate the strength of an ice ridge using known input such as air temperature.

The object of this thesis is to investigate if material properties are substantially different in model scale and full scale. If so, it is desirable to find some kind of coherence between these properties. In this thesis, the focus will be on determining the properties of the unconsolidated layer in the keel, namely the ice rubble. In order to study the material properties, results from punch tests, both full scale and model scale, will be used. The experiments will be recreated in the FEM software Abaqus, using the Coupled Eulerian-Lagrangian approach in explicit analysis. Different values of material properties for the Modified Cam Clay material model will be tried out.

The assignment will be performed in three steps:

1. Modelling of punch tests in the FEM-software Abaqus, both in model scale and full scale
2. Parameter study – fitting of material properties to the experimental results
3. Comparison of ice rubble properties between full scale and model scale

1.1 Structure of the Report

In the following, a presentation of first-year ice ridges will be given along with the challenges of scaling ice rubble properties between model scale and full scale. Thereafter, the theory behind the Modified Cam Clay material model will be explained, following a presentation of the different solutions for the numerical simulation. The use of a Coupled Eulerian-Lagrangian formulation requires the use of explicit analysis, for which the shortcomings, advantages and challenges will be presented. An introduction to the use of the penalty method in contact problems will also be given. Section three provides information about the case study. Herein, the experimental results will be presented and explained. The next sections regard the implementation of the punch tests into the finite element software Abaqus: First, an initial study concerning the energy output in section 4, following a description of the finite element model used for these simulations. Thereafter, the results from the numerical analyses will be presented and compared with the experimental results. Sections 7 and 8 contain a discussion and final conclusions regarding the numerical simulations. Finally, suggestions for further work will be given.

Three appendices are attached. Appendix A is an overview of the analyses from the initial study on the energy balance. Appendix B gives recommendations for Coupled Eulerian-Lagrangian simulations, and Appendix C contains a conversion table between Mohr-Coulomb and Drücker-Prager friction angles.

2 Theory

This section will cover the theory behind first year ice ridges, as well as the challenges that occur when trying to compare model scale to full scale tests. The background for the choices made for the numerical simulations will be given: Herein the Modified Cam Clay material model, the Coupled Eulerian-Lagrangian approach, explicit direct integration and the penalty method for contact problems.

2.1 First-year Ice Ridges

Standard Norge (2010) defines an ice ridge as a *'linear feature formed of ice blocks created by the relative motion between ice sheets'*. These ice phenomena are results of waves, current and wind – when ice floes merge and collide, they are pushed upon each other, often creating so-called rafted layers of ice. Parts of the ice floes will crush, and ice blocks are pushed both above and below the level ice in the interaction. A cross-section of a typical first-year ice ridge is shown and explained in figure 2.1. It consists mainly of two parts:

- The *sail* is defined as the part of the ice ridge that lies above the water line, with maximum height h_s
- The *keel* has maximum height h_k and is the volume of ice beneath the water line. The keel is also divided into two parts: A consolidated layer on top, and below an area of crushed, unconsolidated ice - referred to as ice rubble.

The most common way to define ice ridges is according to their age. *First-year* ice ridges are ridges which haven't yet lived through a summer. If the ice ridge survives one summers melt, it is termed a second-year ice ridge, and further a multi-year ice ridge. In many relevant areas first-year ice ridges prevail, and these are often considered the most critical in engineering.

2.1.1 Formation and Consolidation

Strub-Klein and Sudom (2012) and Høyland (2002) describes the formation and consolidation of ice ridges. Sea ice ridges are results of sea ice drift and deformation, causing ice ridge frequency to be highly dependent on wind conditions. When ice floes merge, the thin ice deforms first. First-year ice ridges are in this way usually created from first-year ice with a thickness

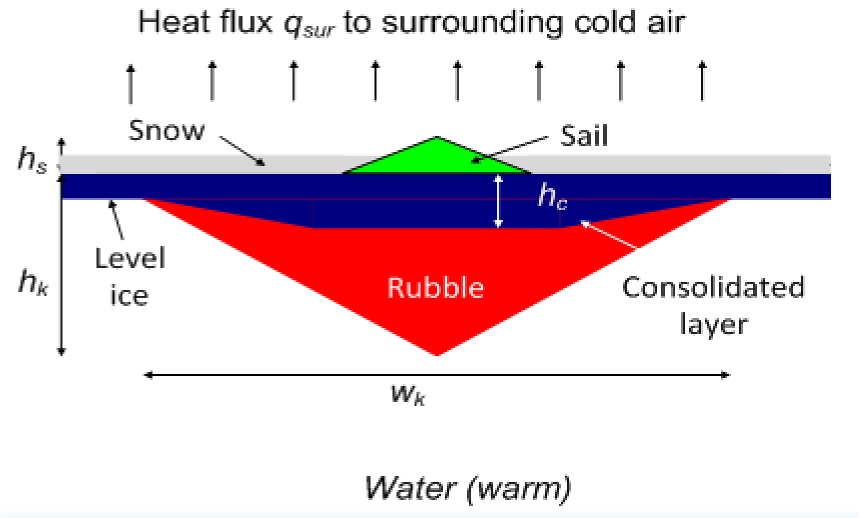

Figure 2.1: *Characteristics of first-year ice ridges (www.ntnu.edu/samcot)*

less than 1 meter. Initially, ice ridges consist of ice blocks piled-up above and below the water line. The ice ridge is then subjected to a consolidation process which is affected by several processes:

- Freezing due to cold air and initial ice temperatures
- Melting due to warmer ocean temperatures
- Redistribution of energy internally
- Insulation due to the snow cover
- Solar radiation

Ice ridges consolidate faster than the surrounding level ice due to the water and slush trapped between the ice blocks in the keel. Cold air and ice temperatures causes the water to start freezing from the water surface. This will eventually create a consolidated layer in the topmost part of the keel, as shown in figure 2.1. The consolidation process proceeds as long as the air temperature is lower than that of the ice. The lower part of the keel will, in contrast, be subjected to a deterioration. The warmer ocean water will melt the ice blocks in the keel, causing it to erode and become softer. At the same time, energy is redistributed internally in the keel by heat fluxes between internal surfaces. Thus, new crystals can be formed at the same time as the blocks become softer. The lower part of the keel will remain unconsolidated, with temperatures approaching the freezing point, T_f, of the ridge material.

The presence of snow plays two parts in the consolidation process. A snow cover will exercise an insulating effect on the consolidated layer, slowing down the consolidation process. An uneven snow cover may in this way contribute to an uneven thickness of the consolidated layer (Høyland, 2002). The snow cover also *contributes* to the consolidation. The pores in the sail are initially filled with air or snow, and when exposed to solar radiation, the sail will erode and snow melts and refreezes in the ice blocks.

The properties of ice ridges in other words vary both in time and space, enhancing the need for thorough investigations.

2.1.2 Ice Ridge Characteristics

In order to make accurate models of ice ridges, geometrical and morphological characteristics, as well physical and mechanical properties are needed. The latter is covered in section 2.1.3 and can be derived from in-situ or laboratory testing. Experiments on ice are not as straight forward as with other materials, and special techniques have been developed. The most common measurements that are made on ice ridges are those related to geometry: Height/depth and width of the sail and keel, and thickness of the consolidated layer and surrounding level ice. More seldom, block thickness of the sail is measured. Keel and sail angles can be measured or derived from height and width measurements.

The sail dimensions are the most frequently reported values. The sail is above the waterline, making it easier to access than the underlying keel. The keel depth is generally much larger than the sail height, and is usually measured by drilling or using sonar devices (Sudom and Timco, 2013). Several attempts have been made to find the relationship between the keel and sail geometries on first-year ice ridges. Standard Norge (2010) claims the ratio of sail height to keel depth (h_s/h_k) to be between 4 and 5, which is comparable to values found in literature (Timco and Burden, 1997; Strub-Klein and Sudom, 2012; Sudom and Timco, 2013). There is, however, a great scatter in the results, emphasized by high reported standard deviations. In this way, the preliminary results can't describe any clear relationship other than the general trend of increasing keel depth with increasing sail height. Sudom and Timco (2013) explains the high standard deviations partly as a result of some ridges having a nearly non-existent sail despite a very deep keel, and partly due to the fact that the maximum depth of the keel is not necessarily located directly beneath the top of the sail.

Keel and sail geometries vary along the length of a ridge, but due to time limitations in field studies, this is generally not investigated. Ridge profiling is often based on picking a cross section with a "classical" shape, as in figure 2.1 (Sudom and Timco, 2013). Although there is little data available, the sail area or volume gives a better indication of keel size than the relationships above (Sudom and Timco, 2013). Timco and Burden (1997) found indications of a linear relationship between the keel and sail *area*, defined by $A_k = 7.96A_s$. Using typical ice densities, this fits well with Archimedes law, saying that the buoyancy is equal to the weight of the water which is suppressed by the ice.

The thickness of the consolidated layer is measured either by drilling or using thermistor strings. Test results show that the thermistor strings give a smaller thickness than what is found by drilling. This is thought to have a connection with the *partly consolidated zone*, which is not accounted for in the thermal definition (Høyland, 2002). The disadvantage of drilling is that the method is highly dependent on the operator, and thereby subjective. The consolidated layer has been estimated to be between 1.6-1.9 m (Høyland, 2007; Strub-Klein and Sudom, 2012), but investigations of Timco and Burden (1997) indicate that the consolidated layer thickness may vary by a factor of more than 3.

A common way to describe the thickness of the consolidated layer is to compare it to that of the surrounding level ice. Standard Norge (2010) states that the thickness may be assumed to be 1.5-2 times the level ice thickness. Sudom and Timco (2013), on the other hand, found evidence that there is no strong relationship. Based on 109 available measurements on both level ice and consolidated layer thickness, they found a mean ratio, h_c/h_{li}, of 3.21, but with a standard deviation as high as 2.83. They claim that the sail block size better correlates to the consolidated layer thickness as it gives a more reliable indication of the level ice thickness when the ridge initially formed.

The porosity of a ridge is an important property in the attempts of defining the strength of the ridge. When defining the porosity of an ice ridge, most articles refer to the macroporosity, η. This is defined as the ratio of any non-ice material to the total volume. The macroporosity is usually measured by drilling. Any drop of the drill is interpreted as a pore. A soft/slushy consistency of the rubble makes investigations difficult, especially late in the season (Høyland, 2002).

Table 2.1 gives ranges of macroporosity from literature for the different parts of the ridge. The values are collected from Høyland (2002).

Keel	33-38 %
Sail	21-24 %
Total	30-35 %

Table 2.1: *Ranges of macroporosity from literature*

2.1.3 Mechanical Properties

Both laboratory and in-situ experiments have been conducted in order to try and retrieve mechanical properties for ice rubble, but there are large discrepancies and the knowledge is thereby still limited. A *unique* strength value for the ice rubble cannot be provided due to the fact that the properties change throughout the season (Høyland, 2007).

The reasons for the discrepancies can be many. Ice rubble strength appears to be dependent on a large amount of properties and conditions, and boundary conditions need to be controlled, both during testing and interpretation of test results. Høyland (2007) describes the measured strength in mechanical testing to be affected by three factors:

1. State of the material
   Most importantly: Temperature and stress- or strain-rate
2. Type of material
   Shape, size and distribution of pores and grains
3. Test set-up, equipment and performance of experiments
   The equipment needs to be suitable for field experiments in harsh environment, and control and measure all relevant parameters independently of external factors

The influence of the scaling of the strength has not been thoroughly investigated (Liferov and Bonnemaire, 2005), and Sudom and Timco (2013) claims that laboratory tests of ice rubble strength cannot be reliably extrapolated to field properties. This is discussed further in the next section.

2.2 Scaling of Model Basin Ridges

Model basin ridges are made with the goal of estimating material parameters, mainly for the dimensioning of ice ridge loads on offshore structures. This raises a need for an appropriate scaling of the material parameters from model scale to full scale, which includes both geometrical scaling and scaling of the mechanical properties and loads.

Several conditions affect the scaling from model scale to full scale. In a model basin ridge, the ridge is confined by the walls of the basin. Repetto-Llamazares (2010), however, reports of experiments being done on model basin ridges shorter than the basin length to investigate the effect of this boundary condition. They refer to Dalane et al. (2009), who found that there was no motion in the ice rubble close to the tank walls, and that the global load seemed to be unaffected by the confinement.

An important challenge in the comparison of model basin and full scale ridges is that the consolidation process differs. Høyland (2010) states that there is more ice growth in model basins. Reports show that the consolidated layer becomes relatively thicker in model scale than in full scale. This is due to the significantly shorter consolidation time in model basins, making the initial phase of the consolidation more important (Høyland, 2010).

The microstructure of the ice also affects the scaling. In model scale, the ice rubble is artificially manufactured, causing different ice fragment sizes and shapes (Heinonen, 2004). No standardized way of producing ice ridges in model tanks has been developed. Different methods for preparing model scale ridges are described in Repetto-Llamazares (2010). The microstructure includes the ice crystal diameter, the size or spacing of brine channels or the size and spacing of gas pockets. In full scale the ratio of the ice thickness to the ice crystal diameter usually is in the order of 10-100. In model scale, where the ice thickness is in the order of cm, it is important to reduce the ice crystal diameter to attain a similar ratio (Høyland, 2015). This is usually done in the basins.

In this thesis material parameters for model scale and full scale ice rubble will be compared using the finite element method. The ice rubble will for both cases be described by the Modified Cam Clay material model.

2.3 Modified Cam Clay

Because of the complicated behaviour of ice, and ice rubble in particular, it has proven difficult finding appropriate models to describe the material. Due to the granular composition of ice rubble, the common approach has been to use models from soil mechanics. Common for soils and ice rubble, and in contrast to other materials, is the possibility of significant volumetric changes when being deformed. The numerical simulations presented in this thesis has been modelled using the Modified Cam Clay material model, which is a soil model originally developed to describe clays.

To describe this material model it is first neccessary to go through the general concepts of pressure dependent, elastic-plastic soil models, including yielding and the equations for plastic deformations. Further the specifics of Modified Cam Clay will be presented by explaining the assumed yield surface and the way this changes with changing pressure.

2.3.1 General Concept

In the following, the stress state is given by two components: p' is defined as the mean effective stress, controlling the deformation and dilatation, and q is the deviatoric, or Mises-equivalent stress, causing distortion.

Elastic-plastic models are used to describe the plastic behaviour when a sample is reloaded to a level higher than the previous maximum load, and thereby experiences further permanent deformations. The previous maximum load level is defined as a *yield point*. The *yield surface* is a combination of principle stresses for which yield occurs, and marks the boundary for the elastic region. Yielding is associated with both plastic *shear strains*, $\delta\varepsilon_q^p$, and plastic *volumetric strains*, $\delta\varepsilon_p^p$ (Wood, 1990).

Modified cam clay, among others, uses parallel effective stress and compression planes to describe the volumetric behaviour. Figure 2.2 shows a yield locus (yield surface) for some sample in the effective stress plane (p'-q) and the normal compression line and unloading-reloading line in the compression plane (p'-ν). The parameter ν is the specific volume, defined as $\nu = 1 + e$, where e is the void ratio (Wood, 1990). It relates to the total volumetric strain as shown in equation (2.1).

$$\delta\varepsilon_p = \frac{-\delta\nu}{\nu} \tag{2.1}$$

Figure 2.2 shows a stress change *inside* the current yield locus, which means that there are only elastic deformations and no yielding takes place.

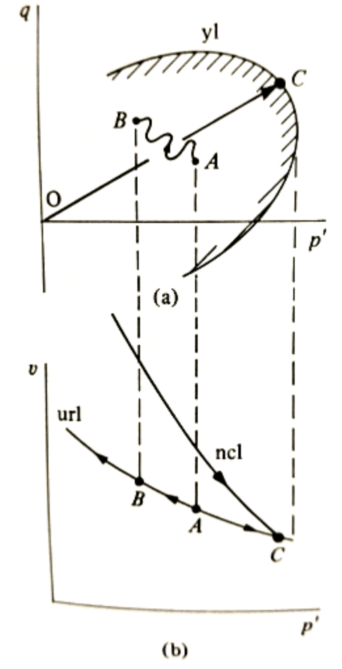

Figure 2.2: *Yield locus (yl), normal compression line (ncl) and unloading reloading line (url) (Wood, 1990)*

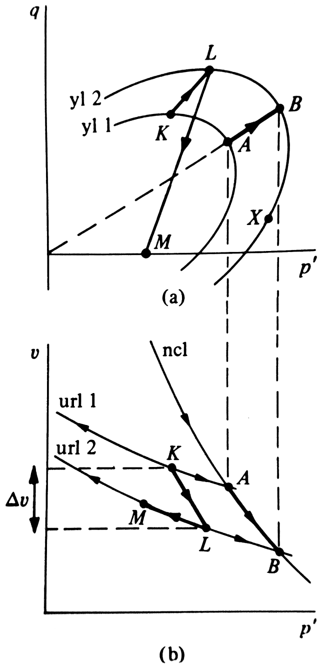

Figure 2.3: *Expansion from yl 1 to yl 2 and corresponding change in unloading-reloading lines (Wood, 1990)*

If the stress changes from a point on the current yield locus to a point *outside* the yield locus, this will cause the soil (or ice) to yield and a new yield locus to form at the point of the new stress state. The new yield locus is assumed to have the same shape as the previous, with only its size changing. In figure 2.3 the stress state changes from K to L, expanding the yield surface from yl 1 to yl 2. The corresponding unloading-reloading lines change from url 1 to url 2 and illustrate the volumetric change by their separation, $\Delta \nu$.

If the normal compression and unloading-reloading lines are plotted with a logarithmic scale on the axis of the mean effective stress, the results will be more linear. An example is shown in figure 2.4. The normal compression line and the unloading-reloading line in the semi-logarithmic plot are defined as shown in equations (2.2) and (2.3), respectively.

$$\nu = \nu_\lambda - \lambda \ln p' \tag{2.2}$$

$$\nu = \nu_\kappa - \kappa \ln p' \tag{2.3}$$

$\nu_\lambda, \nu_\kappa, \kappa$ and λ are as shown in figure 2.4.

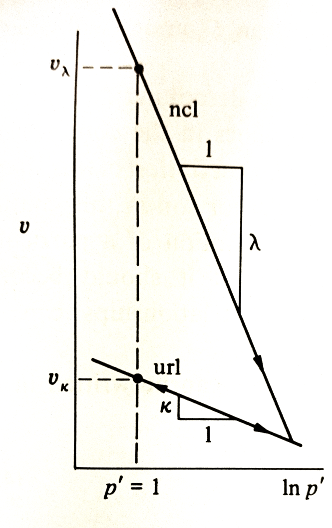

Figure 2.4: *Normal compression line (ncl) and unloading reloading line (url) in lnp'-ν-plane (Wood, 1990)*

The volume change illustrated in figure 2.3 is separated into elastic and plastic deformation:

$$\Delta\nu = \Delta\nu^e + \Delta\nu^p \tag{2.4}$$

$$\delta\nu = \delta\nu^e + \delta\nu^p \tag{2.5}$$

On incremental form, the elastic volumetric changes and corresponding volumetric strain is as defined in equations (2.6) and (2.7).

$$\delta\nu^e = -\kappa\frac{\delta p'}{p'} \tag{2.6}$$

$$\delta\varepsilon_p^e = \kappa\frac{\delta p'}{\nu p'} \tag{2.7}$$

The plastic changes in specific volume and volumetric strain is given in equations (2.8) and (2.9).

$$\delta\nu^p = -(\lambda - \kappa)\frac{\delta p'_0}{p'_0} \tag{2.8}$$

$$\delta\varepsilon_p^p = (\lambda - \kappa)\frac{\delta p'_0}{\nu p'_0} \tag{2.9}$$

Equations (2.7) and (2.9) show that the changes in plastic strain are only affected by the change in the size of the yield locus, p'_0, whereas the elastic strains change whenever the mean effective stress changes (Wood, 1990).

2.3.2 Specifics of Modified Cam Clay

The Modified Cam Clay model is based on the assumptions and equations presented in the previous section. What separates the different elastic-plastic models is the definition of the yield locus and the hardening rule, which defines the way the yield locus changes.

The shape of the yield surface in Modified Cam clay is elliptical and can be identified by equation (2.10), or as the function from equation (2.11).

$$\frac{p'}{p'_0} = \frac{M^2}{M^2 + \eta^2} \tag{2.10}$$

$$f = q^2 - M^2[p'(p'_0 - p')] = 0 \tag{2.11}$$

$\eta = \frac{q}{p'}$ and M defines the shape of the yield locus. M is a soil property depending upon the critical friction angle, as given in equation (2.12).

$$M = \frac{6\sin\phi}{3 - \sin\phi} \tag{2.12}$$

η relates to the *mobilized* friction angle, ϕ_m in the same way.

All possible yield surfaces will go through the origin, and have sizes characterized by the pressure p'_0 at the intersection with the p'-axis. The characteristics of the yield surface is shown in figure 2.5, and figure 2.6 illustrates the effect of change in yield locus.

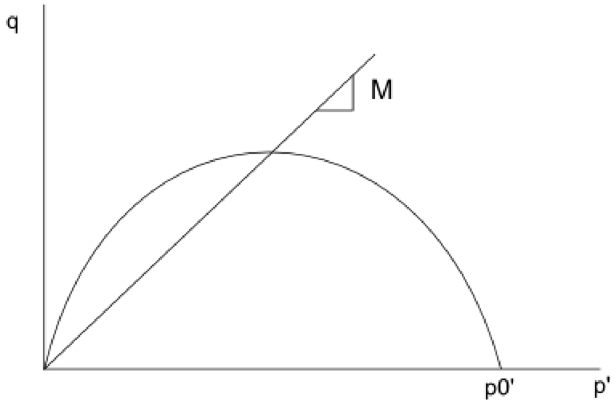

Figure 2.5: *Elliptical Modified Cam Clay yield locus*

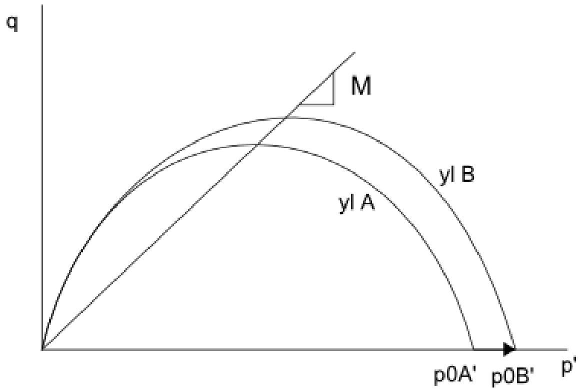

Figure 2.6: *Change in yield locus*

Figure 2.7 shows the boundary of the critical state in the effective stress and compression planes and how these relate to each other, as was discussed in the previous section.

The hardening rule is the same as the *penalty* for increase in p'_0. The Modified Cam Clay model uses a volumetric hardening model; the change in p'_0 is only related to change in *volume*. The hardening rule is defined in equation (2.13).

$$\delta\varepsilon_p^p = \frac{(\lambda - \kappa)}{\nu} \cdot \frac{\delta p'_0}{p'_0} \tag{2.13}$$

The volumetric hardening model restricts the volumetric plastic strains, but

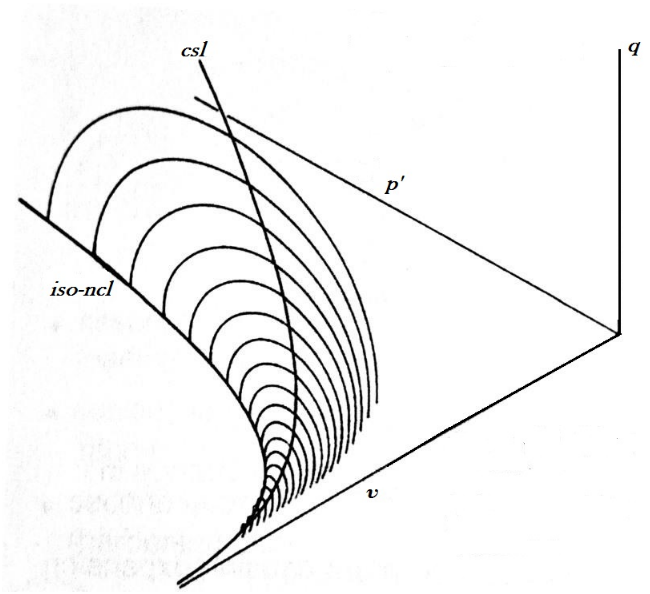

Figure 2.7: *Critical state boundary surface*

the distortional strain is unrestricted and can change indefinitely.

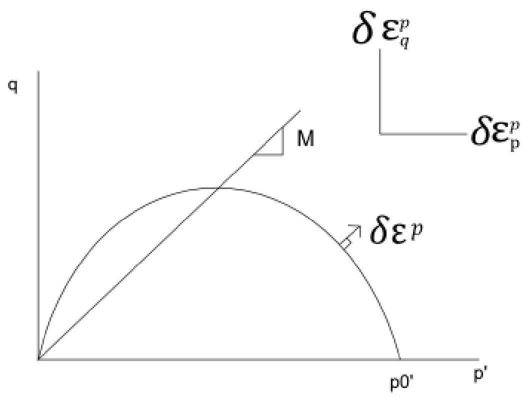

Figure 2.8: *Plastic strain increments*

The plastic distortional strain is given by assuming normality of the plastic strain increments to the yield locus at the current stress state, as shown in figure 2.8. This is called the *flow rule* and is given by equation (2.14).

$$\frac{\delta\varepsilon_p^p}{\delta\varepsilon_q^p} = \frac{M^2 - \eta^2}{2\eta} \tag{2.14}$$

The elastic distortional strain is associated to the change in deviatoric stress q as in equation (2.15).

$$\delta\varepsilon_q^e = \frac{\delta q}{3G'} \tag{2.15}$$

where G' is the shear modulus and remains constant.

The ratio $\delta\varepsilon_p^p/\delta\varepsilon_q^p$ decreases as the stress ratio $\eta = \frac{q}{p'}$ increases. The behaviour of the material in relation to the stress and strain ratio is as follows:

- Plastic hardening - yield locus expands: $\eta < M$, $\delta p_0' > 0$
- Plastic softening - yield locus shrinks: $\eta > M$, $\delta p_0' < 0$
- Perfect plasticity: $\eta = M$, $\delta p_0' = 0$

The critical state, $\eta = M$, means that the material is continuing shearing without further change in stress or volume.

The perks of the Modified Cam Clay Model is that the stiffness formulation always works: A strain increment gives a stress increment. The elastic stresses are predicted and then followed by a plastic correction if the predicted values exceed the yield surface. Numerical errors may, however, occur if there is softening. If the same stress range is associated with both plastic and elastic strain, bifurcation of the response may occur when unloading.

2.4 Numerical Simulation of Ice Ridge Action

Out of the different numerical methods, simulations of ice ridge action are mainly performed by either of two methods: 1) Discrete Element Method (DEM), or 2) Finite Element Method (FEM). Discrete modelling has the advantage that it captures the basic composition of ice rubble: The keel is considered an assembly of discrete particles, with freeze-bonds and contacts accounted for. Equations of motion are solved for each ice block, and forces and displacements are retreived using specific contact formulations (Serré, 2011).

Discrete modelling is, however, not as much used for industrial purposes. Despite its theoretically good fit for ice rubble simulations, the method demands algorithms and contact properties to be customized for the specific purposes. For these reasons, Finite Element modelling may be a more efficient tool for ice load calculations. In Finite Element modelling, the ice rubble is considered a continuum and homogeneous material. Serré et al. (2013) states that the ratio of the average particle size to the average rubble depth often is quite low (around 10), due to the large porosity of ice rubble. In this way, the use of continuum mechanics may be inaccurate. However, previous simulations of punch through tests on ice rubble using the Finite Element Method have successfully managed to fit the experimental behaviour and load magnitudes (Serré et al., 2013).

This thesis is based upon numerical simulation in the Finite Element Software Abaqus. In the following, the different solutions used for the numerical simulation are described.

2.4.1 Explicit Method in Numerical Analyses

Performing a numerical analysis includes the choice between an implicit or an explicit integration method.

In explicit methods, the solution u_{i+1} at time t_{i+1} is determined by evaluating the dynamic equilibrium equation (2.16) at time t_i (Chopra, 2007). Known displacements u_i and u_{i-1} are used to compute the next displacements.

$$m\ddot{u} + c\dot{u}_i + ku_i = p_i \tag{2.16}$$

For implicit methods, the displacement u_{i+1} is determined from equation (2.17) at time t_{i+1}. This is equivalent to evaluting equation (2.16) at time t_{i+1} in stead of t_i (Chopra, 2007), and requires both equation solving and equilibrium iterations.

$$m\Delta\ddot{u}_i + c\Delta\dot{u}_i + k\Delta u_i = \Delta p_i \tag{2.17}$$

The explicit method is ideal for high-speed dynamic events, but can also be applied to slower quasi-static problems. Also, the explicit solution procedure is preferable for contact problems. Implicit methods are preferable when the response period of interest is long, or the nonlinearities are smooth (Mathisen, 2014*b*). The advantage of implicit procedures are that they are unconditionally stable, i.e. they are stable for any time increment size. The use of a coupled Eulerian-Lagrangian formulation is only available in Abaqus/Explicit.

Abaqus uses the Central difference method for explicit integration, which is based on a finite difference approximation of the velocity and acceleration.

The advantages of the explicit procedure is that, as opposed to implicit procedures, equation solving and equilibrium iterations are not neccessary, excluding the issue of convergence and making each time step computationally inexpensive. The disadvantage is that the method is only conditionally stable, meaning that the method is stable only for time steps smaller than a certain critical time step. The critical time step is defined in equation (2.18).

$$\Delta t_{cr} = \frac{L^e}{c_d} \tag{2.18}$$

L^e is the smallest element length present in the model, and c_d is the dilatational wave speed in the material, defined as in equation (2.19). E is Young's modulus and ρ is the material density. The critical time step will be small for a very refined mesh, a large Young's modulus or a small material density.

$$c_d = \sqrt{\frac{E}{\rho}} \tag{2.19}$$

When solving nonlinear dynamic problems with the explicit method, the energy balance needs to be monitored in order to detect possible numerical instability. Numerical instability may be dissipated by energy-dissipating nonlinear material behaviour, which can make the solution seem reasonable even if it's not (Mathisen, 2014*b*).

2.4.2 Energy Balance in Abaqus/Explicit

The sum of all energy components, i.e. the total energy, should be constant throughout the analysis. In a Finite Element model, however, it will only be approximately constant, but should be of an error less than 1%. For the simulations in this thesis, the total energy can be summed up as in equation (2.20).

$$E_{tot} = E_I + E_K + E_V + E_F - E_W - E_{PW} \tag{2.20}$$

E_I is the internal energy, E_K is the kinetic energy, E_V is the viscous dissipation, E_F is the frictional dissipation, E_W is the external work and E_{PW} is the internal work by penalty contact. The latter is described in section 2.4.4.

The artificial strain energy, meaning the energy introduced by hourglass control, and the damping dissipation (E_V) should be negligible compared to the physical energies such as strain energy and kinetic energy. In quasi-static analyses, the kinetic energy should only be a small fraction of the internal energy (Dassault Systémes, 2012*a*).

When the analysis involves contact or constraints, the contact penalty work and the constraint penalty work should also be monitored. These energies should be close to zero (Dassault Systémes, 2012*a*).

The energy output for Eulerian analyses may be misleading since material can enter and leave the domain - material loss will result in loss of energy and material flowing into the region will give a corresponding increase in energy (Dassault Systémes, n.d.).

2.4.3 Coupled Eulerian-Lagrangian Formularion (CEL)

The numerical models in this thesis are made with a Coupled Eulerian-Lagrangian (CEL) formulation, which means that a Lagrangian mesh is used to discretize the structure, while a Eulerian reference mesh is made for the ice rubble.

In the Lagrangian description, all physical quantities are expressed in terms of the time t and their *initial* position. The nodes are fixed within the material, causing the mesh to be highly distorted for high strain gradients. In the Eulerian approach, strains, stresses and displacements are functions of time and their *current* position. The nodes stay fixed while the material flows through the mesh, ensuring that no element distortion occurs. The disadvantage of the Eulerian formulation is that it cannot describe the interface between two parts as precicely as the Lagrangian formulation.

The advantage of CEL is that one utilizes the advantages of both methods: Using the Lagrangian formulation the interface between the structure and Eulerian mesh is precisely defined, while the Eulerian mesh can handle large deformations and remains undistorted. The Eulerian mesh is fixed and traces the material particles, keeping track of the material boundaries throughout the analysis (Qiu et al., 2009). The initial material location is defined inside the Eulerian mesh, while the rest of the mesh is defined as initially being void. The interface between the two parts can be defined at the boundary of the Lagrangian structure, while the interaction between them is imposed by a general contact definition (Dassault Systémes, 2012*b*). In explicit analysis, the penalty method is used for this purpose, as explained in the next section.

The accuracy of an Eulerian model can typically be a bit less than the accuracy of a Lagrangian model with the same mesh density. This is mainly due to the estimations that are made when tracking the material boundaries within partially filled elements, and the estimations in the advection process that maps the state of the elements within the fixed mesh (Dassault Systémes, n.d.).

2.4.4 Penalty Method for Contact Problems

In the numerical simulation of the punch tests, the interaction between the rigid structure and the ice ridge introduces a contact problem. Contact is a geometrically nonlinear problem which occurs with contact, separation or sliding between structures, or between different surfaces on the same structure (Cook et al., 2002). Contact problems are often highly nonlinear due to large and rapid stiffness changes when surfaces come in contact.

In Finite Element Analyses (FEA) contact forces are transmitted between surfaces with special kinds of nonlinear, discontinuous constraints. The constraint is applied only when the surfaces are in contact. The options for solution procedures in contact problems are many, the most common being the Lagrange Multiplier Method, the Penalty Method and the Augmented Lagrange Method. With the use of Abaqus/Explicit, however, only the penalty method is available.

The contact condition in the penalty method is guarded by $\lceil \alpha \rfloor$, which is a diagonal matrix consisting of penalty numbers α_i, also denoted the penalty stiffness. The penalty for violating a constraint increases with increasing penalty numbers (Cook et al., 2002). Small values of $\lceil \alpha \rfloor$ leads to the constraints being ignored, and for large $\lceil \alpha \rfloor$ the constraints are nearly satisfied. The penalty method will never completely satisfy the constraints. A small value of the penalty stiffness may yield inaccurate results, yet a large value may provoke numerical error as well as increase the computational time (Mathisen, 2014*a*). With Abaqus/Explicit, the values of α is automatically maximized subject to stability limits (Dassault Systémes, 2012*a*).

This section has covered the main theory behind the punch tests that are simulated - both in terms of ice ridges and the solutions for the numerical simulation. The next section will provide more detailed information on the punch tests themselves.

3 Case Studies

Results from previously performed punch tests are collected in order to study the effect of different material properties on the results, and to try and approach the experimental results in the numerical simulation. Both full scale and model scale punch tests have been studied. The intention of the punch test is to load the ridge keel in order to retrieve its mechanical properties.

3.1 Model Scale Punch Tests

Model scale punch tests are executed in a basin with either artificial fields of ice rubble, level ice or ice ridges. Figures 3.1a and 3.1b shows two different examples of model scale punch tests - one with a large circular loading plate, and one using a small cylinder. The latter has been the most frequently used in the latest years since one avoids the possibility of ice appearing at the top of the plate. The large loading plate test (Figure 3.1a) is used for the purpose of this thesis.

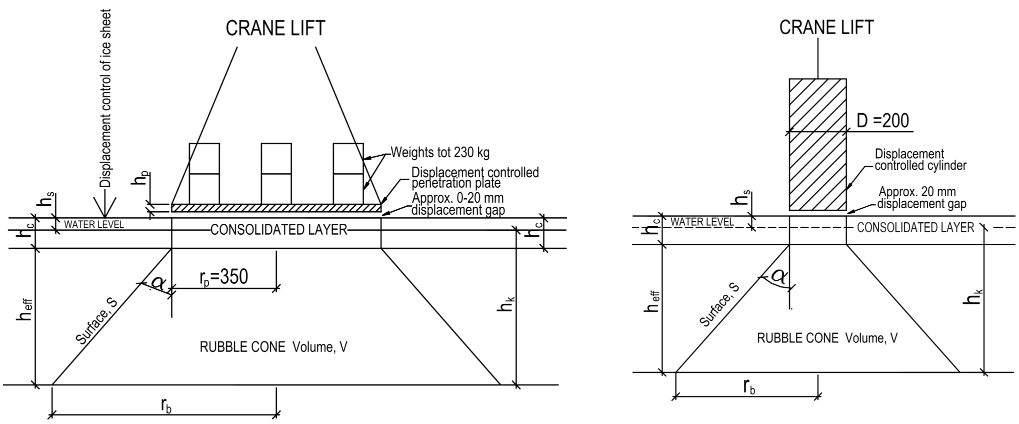

(a) *Large plate* **(b)** *Small cylinder*

Figure 3.1: *Principle of punch tests in model scale (Jensen et al., 2001b)*

The model scale punch tests subject to this thesis were conducted in 2001 in the large ice tank at the Hamburg Ship Model Basin (HSVA). Six ice ridges were produced out of three ice sheets (#1000, #2000 and #3000) (Jensen et al., 2001*a*). The ridges were prepared by pushing ice sheets against a transverse beam. The beam was moved forward, about 0,6 meters at a time, to create the rubble. Level ice was eventually pushed above (final rafting) to form a ridge with the desired width and keel depth (Jensen et al., 2001*a*). Figure 3.2 gives an illustration of the process. An uneven thickness in the tank is reported - probably due to mechanical deformation in connection with sampling.

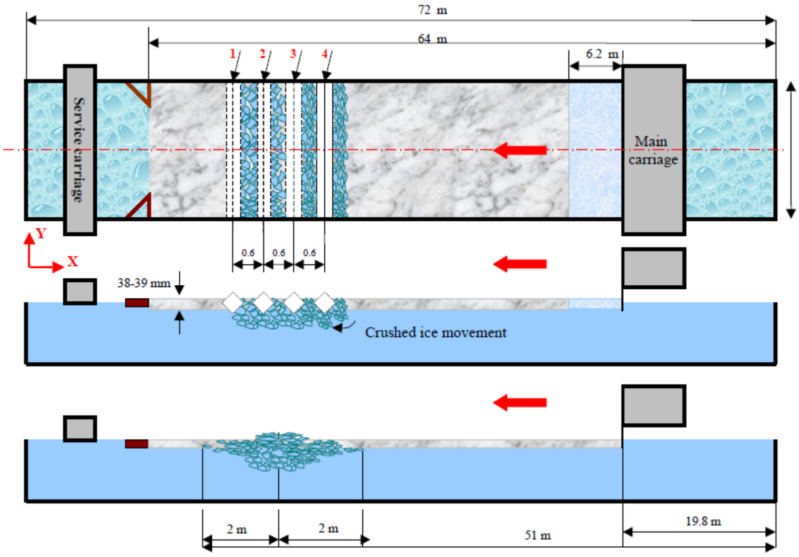

Figure 3.2: *Preparation of the model scale ice ridges (Jensen et al., 2001a)*

After preparation of the ice ridges, salinity and density was measured and the temperature development was logged from thermistor-strings. The density was measured by taking samples from the sail.

Three types of push down (punch) tests were executed: using a large circular loading plate, a small circular loading plate and a rectangular loading plate ("2D" tests), adding up to a total of 37 single tests. During preparation, the sail was removed from the model ridge and the consolidated layer was cut free from the surrounding ice along the perimeter of the plate (Jensen et al., 2001*b*). The punch tests consisted in lowering the loading plate with a velocity of approximately $v_p = 7mm/s$ at the center of the ridge until failure had developed through the entire keel, before lifting the plate and then lowering it again. The tests simulated in this thesis were executed using the large loading plate, as in figure 3.1a. The loading plate had a diameter of 0.7 meters and was loaded by 175 kg of steel weights. A load cell measured the resistance of the keel, and two displacement sensors measured the displacement of the penetration plate (Z1) and of the surrounding ice

(Z2) (Jensen et al., 2001*b*).

Tests 3001CL and 3002CL on ridges 3001 and 3002 were chosen for the numerical simulation. Ridge 3001 was made from warm level ice and ridge 3002 from cold level ice. The tests were both executed at the center of the ice tank with a large plate, cf. the C and L in the test names. Table 3.1 gives the properties of the ridges, collected from Jensen et al. (2001*a*) and Jensen et al. (2001*b*). The cut depth is only announced for the tests on ridge 3002. A cut depth of 0.13 m is assumed for the test on ridge 3001. The ice density is assumed to be equal to the measured density for the sail blocks. It is taken as an average of two different measurement methods, described in Jensen et al. (2001*a*), and assumed equal for the two ridges as they originate from the same ice sheet. The rubble density is calculated from equation (5.5) assuming a water density of 1000 kg/m^3. Figures 3.3, 3.4 and 3.5 show cross sections of ridges 3001 and 3002 taken from the centre of the ice tank.

Ridge #	3001 Warm level ice	3002 Cold level ice
Test name	3001CL	3002CL
File name	D310101T111454	D310101T171452
Average ice density [kg/m^3]	887	884
Average porosity [%]	47	36
Rubble density [kg/m^3]	939	926
Average keel depth [mm]	400	700
Cut depth [mm]	130*	180
Depth of consolidated layer [mm]	88-124	103-138
Diameter of plate [m]	0.7	0.7

*Assumed

Table 3.1: *Test data for model scale punch tests*

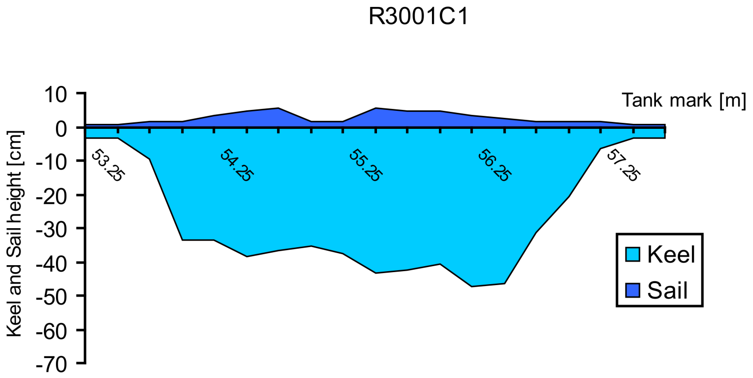

Figure 3.3: *Cross section of ridge 3002 at the center of the tank, profile 1*

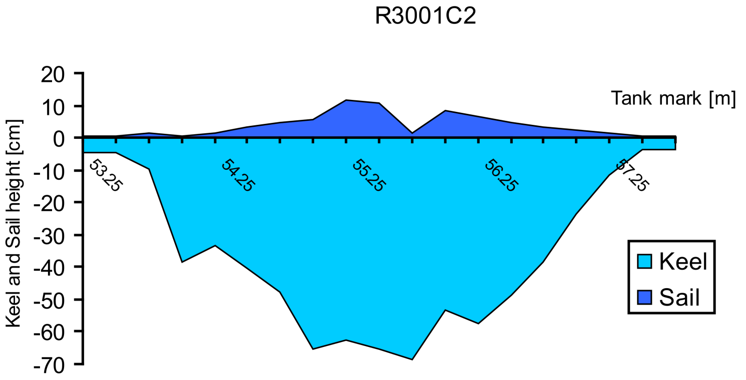

Figure 3.4: *Cross section of ridge 3002 at the center of the tank, profile 2*

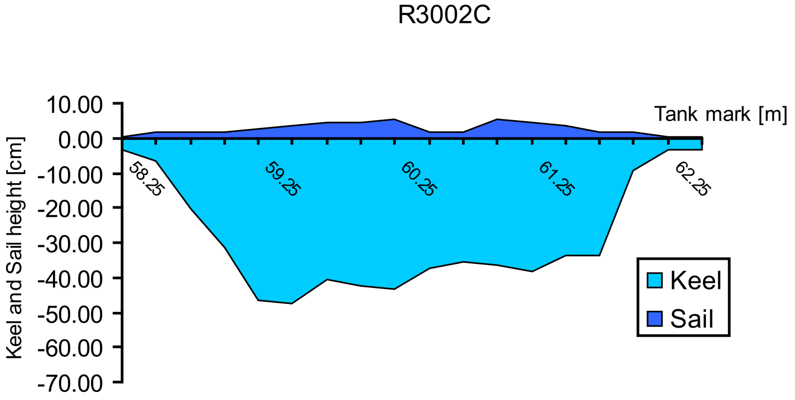

Figure 3.5: *Cross section of model scale ridge 3002 at the center of the tank*

Figures 3.6 and 3.7 gives the reaction force and displacement against time for punch test 3001CL and 3002CL, respectively. The displacement is calculated as the difference between measured displacements Z1 and Z2 to exclude the displacement of the level ice surrounding the plate. Net force F_z is net vertical force in the load cell between the crane and the plate, minus buoyancy from the equipment. The reaction force is increasing continuously as the plate is lowered with constant velocity onto the ridge. When the plate is lifted again, the reaction force sinks, reaching a minimum value as the movement is reversed. When the plate is lowered again, the reaction force reaches a new maximum level. The almost vertical increase in the second peak force of test 3001CL is caused by a large increase in velocity in this time interval.

The force has for both tests an initial value of about 400 N, which represents the zero-value for the load cell. The load cell measures tension and should give zero when the foundation holds all the loading. For test 3002CL, especially, the force sinks lower than the initial 400 N at the middle of the time interval. This should indicate additional weight on the plate and may be caused by ice gathering on top of the plate. Figure 3.7 shows that the plate is lowered 163 mm in the first step, which is more than the reported maximum thickness of the consolidated layer from table 3.1. Thus, there is a possibility for ice to float on top of the plate. A difference of 100 N equals about 10 kg of ice, which is not unlikely. The negative values for the reaction force is further ignored.

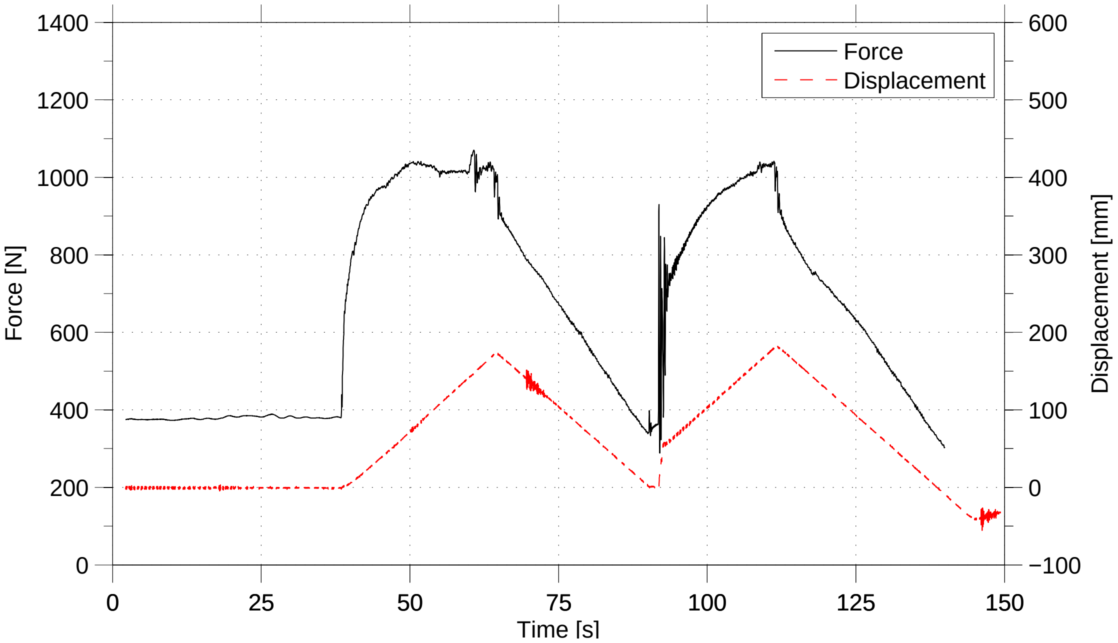

Figure 3.6: *Model scale punch test on ridge 3001, experimental results*

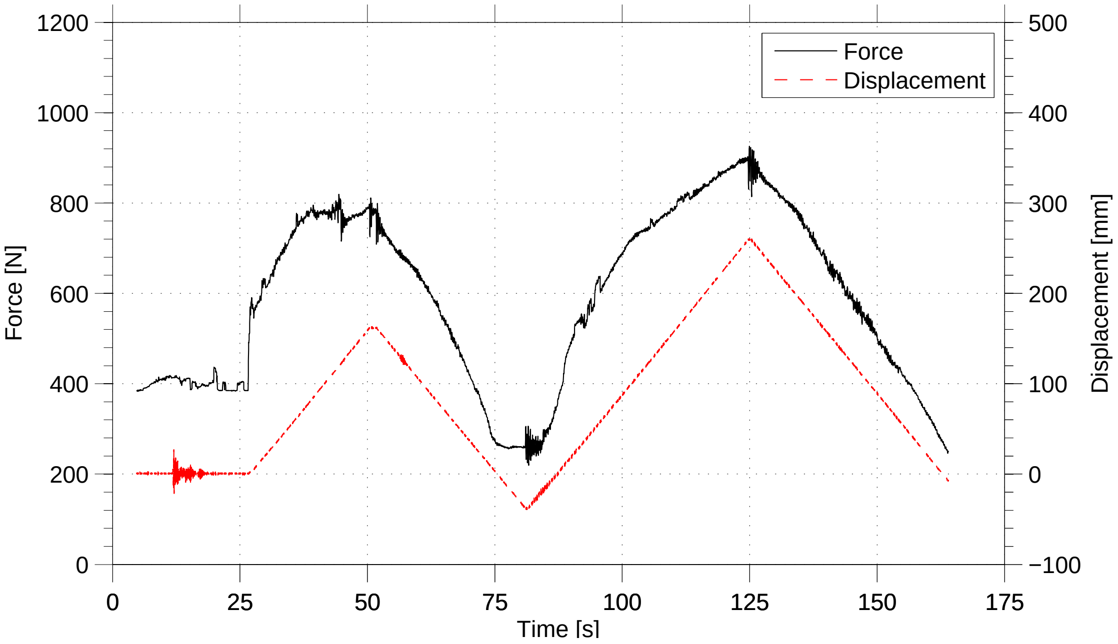

Figure 3.7: *Model scale punch test on ridge 3002, experimental results*

3.2 Full Scale Punch Tests

The full scale punch tests that are subject to this thesis were conducted in 1999 in Hailuoto in the Gulf of Bothnia, Finland. 4 tests are chosen for numerical simulation. They were done as a part of the doctoral thesis of Jaakko Heinonen (Heinonen (2004)). A total of 12 punch tests were performed by Heinonen and Määttänen between 1998 and 2001.

A new test set-up was designed and manufactured especially for these tests. A principle sketch of the set-up is shown in figure 3.8. A hydraulic actuator with a capacity of 1 MN was used to load the ridge. The loading rig had a 9 m tall mast which was fixed to the surrounding level ice using ice anchors, coupled to the mast with up to 20 couples of steel wire ropes. A more thorough explanation of the hardware and instrumentation is provided in Heinonen (2004).

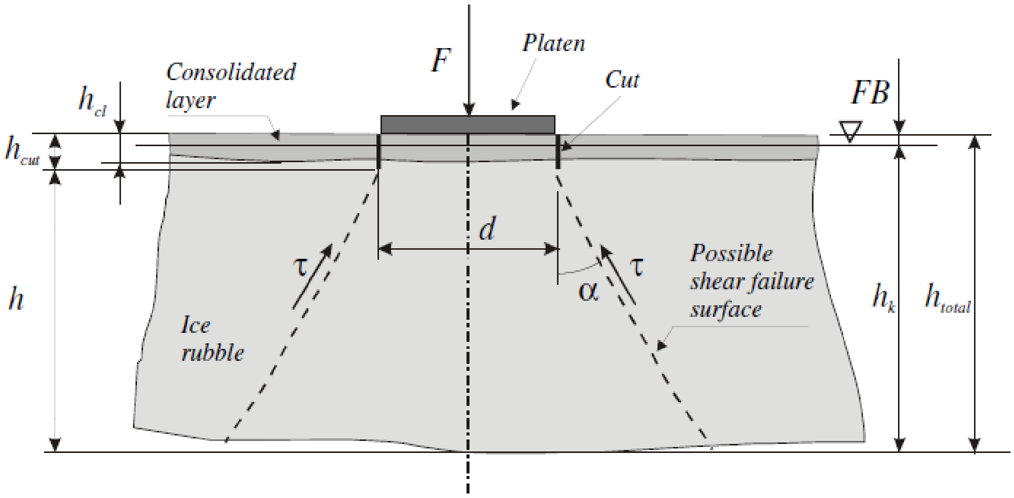

Figure 3.9: *Principle sketch of full scale punch test (Heinonen (2004))*

In these full scale punch tests, the keel was loaded by a circular platen pushed downwards. A constant velocity of the platen was targeted, although this is difficult when using hydraulic systems, especially when approaching maximum capacity of the system. In order to load only the ice rubble, the snow and sail of the ridge was removed prior to testing. A circular cut was made through the consolidated layer using a chainsaw, to separate it from the surrounding ice field. This was done both in order to reduce the load capacity required, and to more easily isolate the contribution from the ice rubble to the total load. Wooden beams were placed on top of the consolidated layer

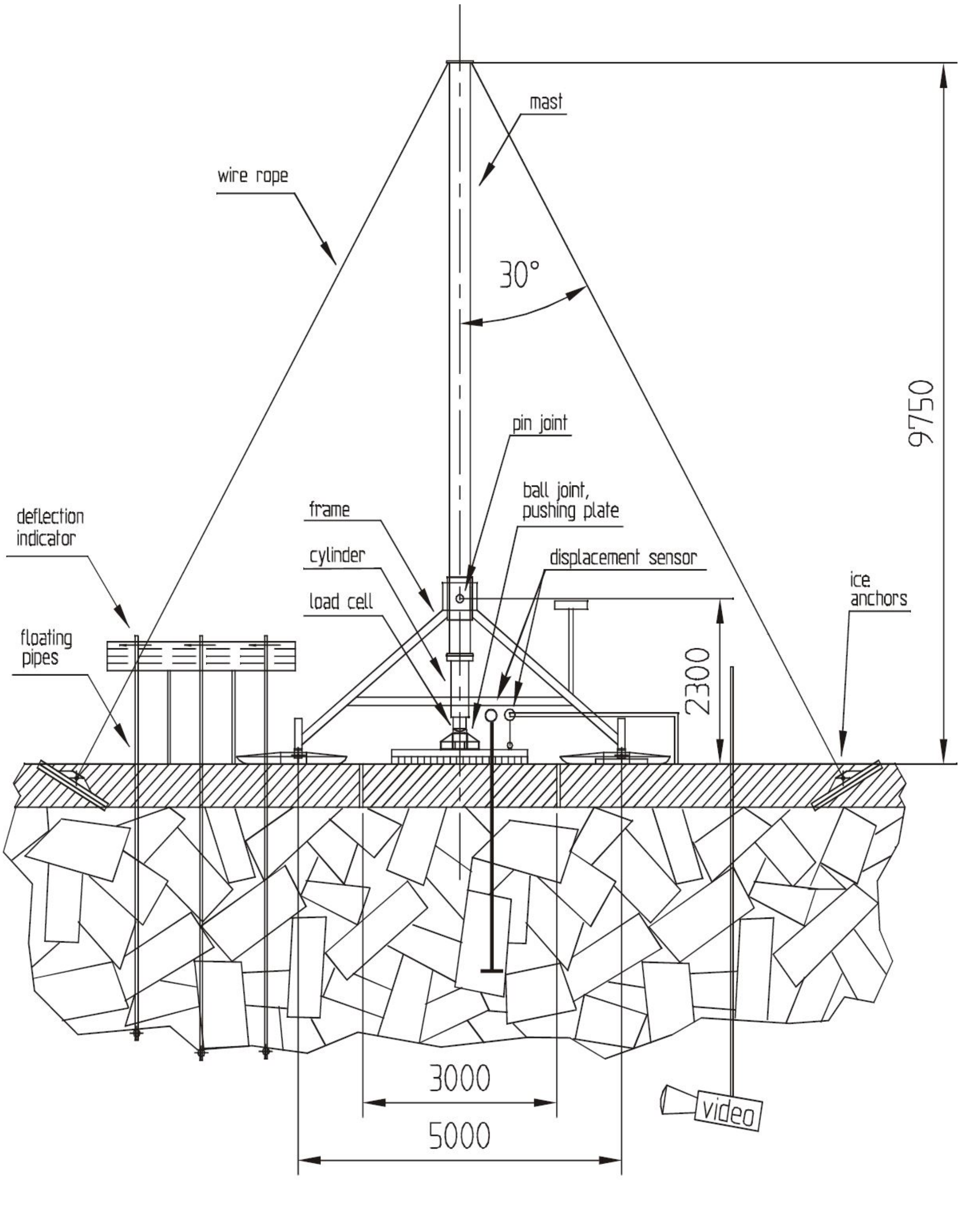

Figure 3.8: *Principle sketch of the full scale punch test equipment (Heinonen (2004)). Dimensions in mm*

to retrieve an even load distribution (Heinonen, 2004). A principle scetch of the punch test is shown in figure 3.9.

For each test site, the porosity of the keel was determined, as well as the distribution of the keel thickness and freeboard. A summery of the test data is given in table 3.2. The numbers of the tests are the same as used by Heinonen. The keel depth is measured from the water surface. An effective keel depth, reaching from the bottom of the cut to the bottom of the keel, can be calculated as in equation (3.1). The cut depth is further interpreted as the thickness of the consolidated layer in lack of accurate measurements, meaning that the effective keel depth equals the depth of ice rubble. The density of ice rubble in table 3.2 is determined from equation (5.5).

$$h_{eff} = h_r = h_k + FB - h_{cut} \tag{3.1}$$

Several values were recorded during the testing: The force F pushing the platen downwards, the platen displacement u, the compaction Δu of the rubble and the displacements at the bottom of the keel. The experimental results for the reaction force and platen displacement are presented in figures 3.10 through 3.13.

Test number	2	6	9	10
Date	02.03.1999	04.03.1999	15.03.1999	17.03.1999
Average porosity [%]	34	27	31	42
Ice density [kg/m^3]	932	932	932	932
Rubble density [kg/m^3]	955	950	953	961
Average keel depth [m]	4.55	3.89	5.99	4.47
Average freeboard [m]	0.2	0.26	0	0.06
Cut depth [m]	0.8	1.5	1.6	1.4
Effective keel depth [m]	3.95	2.65	4.39	3.13
Diameter of plate [m]	3.32	3.35	3.4	4.5

Table 3.2: *Test data for full scale punch tests*

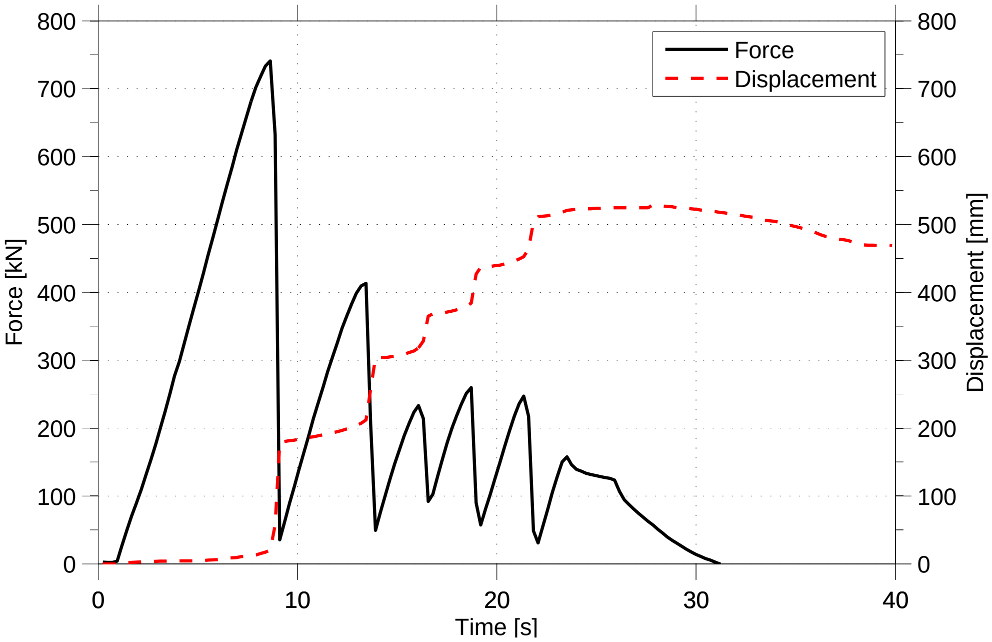

Figure 3.10: *Full scale test 2, experimental results*

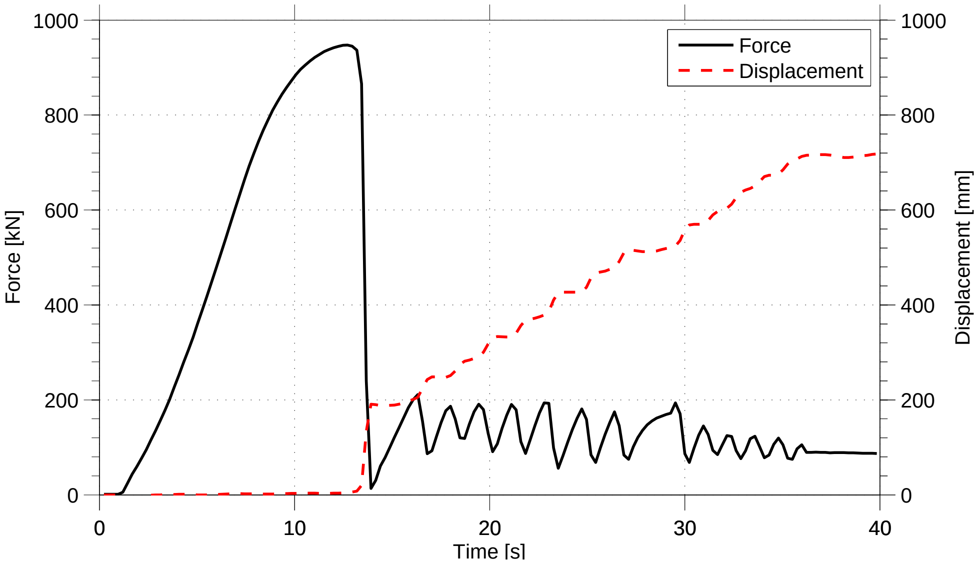

Figure 3.11: *Full scale test 6, experimental results*

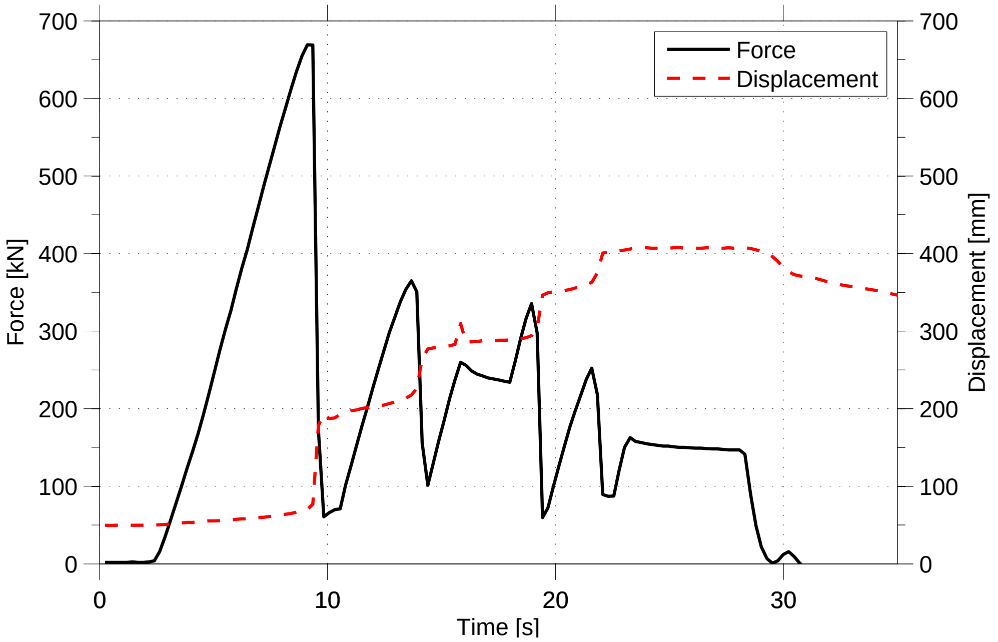

Figure 3.12: *Full scale test 9, experimental results*

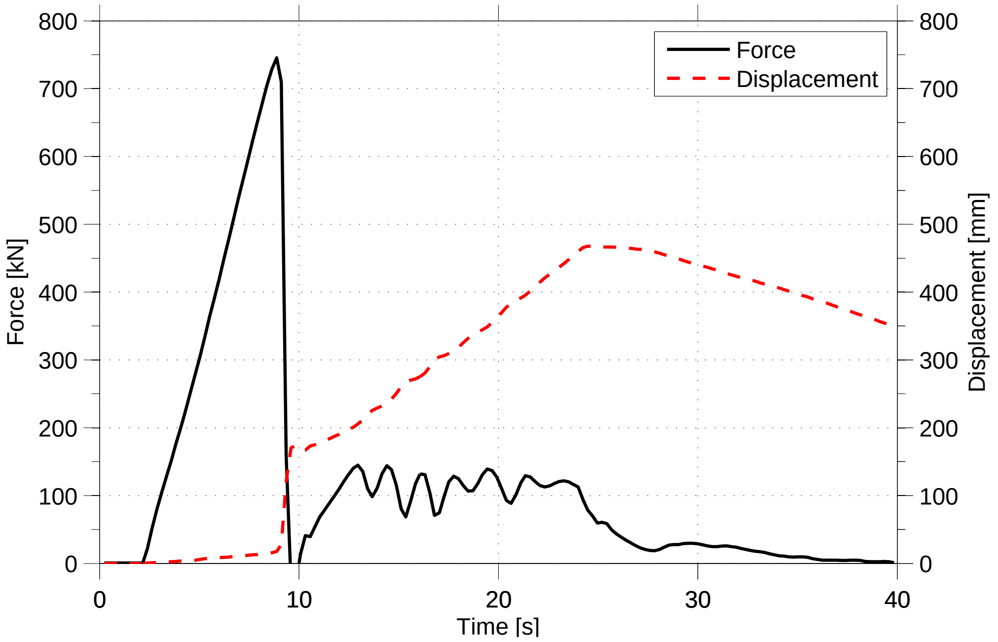

Figure 3.13: *Full scale test 10, experimental results*

Heinonen (2004) claims that the first peak of the reaction force is due to breakage of the skeleton structure. The subsequent peaks are partly due to the failure of individual floes, and partly due to rearrangement of the ice blocks.

He also explains that due to the control system not receiving any feedback information, the platen velocity was not exactly constant during large load drops. The velocity was lower before global keel failure than afterwards. In addition, the steel wire ropes in the test rig store lots of strain energy that is released when the keel fails, i.e in the post peak region of figures 3.10 through 3.13. This causes larger force drops and a higher displacement rate after the first failure.

Heinonen (2004) calculated an average shear strength by assuming a cylindrical failure surface. For test 6, this shear strength was so high that he debates that the cut cannot have reached through the whole thickness of the consolidated layer.

Permanent movements of both the platen and the keel bottom was observed, supporting the use of plasticity theory for the numerical model (Heinonen, 2004).

4 Initial Study - Energy Imbalance

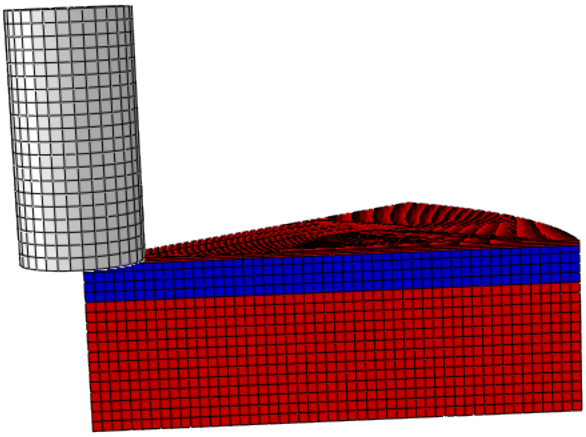

Figure 4.1: *Geometry of model from initial studies (Nilsen, 2014)*

4.1 General

Prior to this thesis, a project study was carried out on a simpler model consisting only of ice rubble, loaded by a bottom closed cylinder. The geometry of the model is shown in figure 4.1, where the blue region represents the ice rubble. Symmetry is utilized by only modelling 1/8 of the problem. The punch test simulations, described in Nilsen (2014), showed that the energy balance was not satisfied. As discussed earlier, imbalance in the energy equations may indicate numerical instability and thereby misleading results. Since the simulations in this thesis is based on the same modelling techniques and materials, it was necessary to locate the sources of error and find ways to improve the results.

Figure 4.2 gives a plot of all the major energy contributions in the simulation from the starting point. Internal energy and external work are not in equilibrium. The artificial strain energy is too large and the contact penalty work is nowhere near zero - even growing larger than the external work halfway into the analysis. A similar problem with the penalty work was experienced by Levanger (2012), although his simulation considered a punch test on a steel plate. In the figure E_I is the internal energy, E_{PD} is the plastic dissipation, E_W is the external work, E_{PW} is the internal energy by penalty contact and E_A is the artificial strain energy. Output was requested for the integrated mass, showing that only 0.003 % of the total mass is lost during the whole analysis, meaning that the energy balance should not be misleading, as discussed in section 2.4.2.

An energy study has been carried out to investigate the effects of different modelling techniques and input parameters on the energy output, focusing on improving the energy balance and with that the reliability of the results. The findings are further used in the numerical simulations of model scale and full scale punch tests.

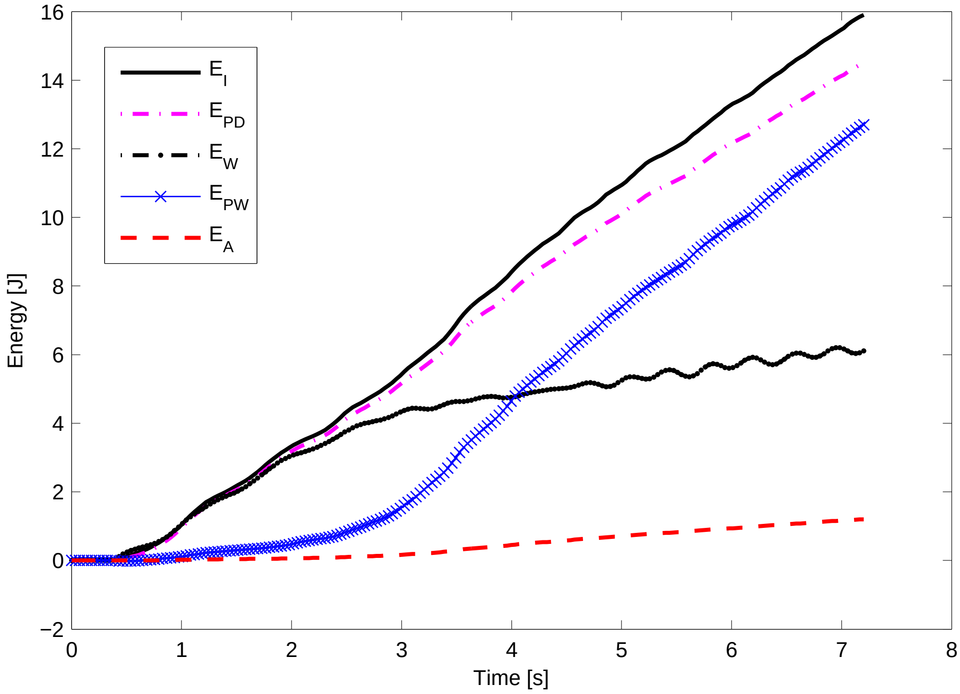

Figure 4.2: *Energy output, initial studies. E_I=internal energy, E_{PD}=plastic dissipation, E_W=external work, E_{PW}=internal energy by penalty contact and E_A=artificial strain energy.*

An overview of the different analyses is given in Appendix A. The impact of meshing techniques and mesh density, geometry, contact definition, material definition, boundary conditions and time increment has been investigated. The most effective remedies proved to be 1) reducing the penalty stiffness, 2) a regular mesh, refined in the region of largest material movement and 3) rounding off the bottom edges of the puncher. A discussion of the effect of the different approaches will be given in the following.

4.2 Hourglass Control

One of the main drawbacks of the simulation is that it experiences high artificial strain energy. When using default hourglass control, which in this case is viscous hourglass control, the artificial strain energy is as much as 30 % of the internal energy. The use of stiffness based hourglass control reduces the artificial strain energy by 82 % at the end of simulation to about 7 % of the internal energy. This is still more than the recommended 1-2 %. The use of stiffness based hourglass control also affects some of the other energy output in the following ways:

- The frictional dissipation increases by 42 %
- The internal energy is approximately the same, though it is now increasing almost linearly throughout the analysis, as opposed to showing a larger increase in the last 2.5 seconds for default hourglass control. A linear increase is more natural for the given interaction
- The internal work by penalty contact has the same values at the start and end of simulation, with larger values for stiffness based hourglass control between 2.5 and 6.5 seconds
- Viscous dissipation is 33 % larger at the end of simulation
- The external work is decreased by 29 % at the end of simulation. For both analyses the external work shows an unexpected oscillation towards the end of simulation
- The total energy, which is almost constant for viscous hourglass control, is decreasing constantly from the start of the analysis. It is worth noticing that when comparing the total energy to the other energies, it may for both cases by considered close to constant, going from 0 to -0.40 J for the case of stiffness based hourglass control

The Abaqus Analysis User's Manual (Dassault Systémes, 2012*a*) states that the stiffness approach is recommended for both quasi-static and transient dynamic simulations. The viscous approach is effective for high-speed dynamic simulations, but is not recommended for low frequency dynamic or quasi-static simulations. Due to the slow loading-rate, stiffness based hourglass control should be preferable.

Considering the large amount of artificial strain energy for viscous hourglass control and the relatively constant total energy for both cases, the stiffness based hourglass control seems to be the best choice. The reaction force also shows a more realistic behaviour with less oscillations, though the differences are minimal. Nevertheless, it is a huge disadvantage that the external work is decreasing, increasing the difference between the external work and the internal energy which preferably should be equal. A combination of the two mentioned hourglass controls is available, where one can specify the weighting, but reducing the effect of the stiffness based hourglass control would be on the expense of again increasing the artificial strain energy.

4.3 Material Definition

Analyses have been run with different types of material to check if the bad results are outcomes of the material definition. Pure elastic material has been tried, as well as a Von Mises material model with both common metal properties and assumed ice properties. For the elastic material, the energy balance is better than before. The internal energy, strain energy and external work are close to being equal. Nevertheless, the values are not close enough. The penalty work is still too large, though no longer larger than the external work, and the viscous dissipation has a greater contribution. As the material did not experience plastic strains, the simulation with a Von Mises material model with ice properties gave the same results as the elastic simulation. The use of Von Mises with metal properties gave bad results. The stable time increment was much smaller than for the other analyses, and the simulation was not completed. The energy values at the start of the simulation showed great variation and was very different from the other simulations.

To check if the errors are results of bad hardening parameters, an analysis has been run with hardening parameters commonly used for clay. These are quite larger than the ones used in the project work, but does not change the results significantly.

The simulations with different material models showed that the problem was not with the material model, nor the hardening parameters. The other material models gave much higher energies than the ones produced using Modified Cam Clay, but this is rather due to the material not experiencing plastic strains than the material model itself. The plastic strains are dissipating energy, giving lower energy values and especially affecting the external work. The internal energy balance is no better for either of the material models

- the only difference is that the plastic dissipation is replaced by the strain energy.

It may be that the energies in the Cam clay model are actually just too small, and thereby causing numerical difficulties for the software. This is emphasized by the fact that the penalty work is actually larger than the external work about half way into the simulation. When the plastic strains are absent, the energies are way higher, giving a penalty work much less than the external work. The ice material has a low density and stiffness, which may be the reason for the large penalty work appearing despite higher energies. This is discussed further in section 4.6.

4.4 Boundary Conditions

A smooth step amplitude was added to the constant velocity boundary condition. This options applies the load gradually to avoid a sudden impact loading on the deformable body (Dassault Systémes, 2012*a*), and is recommended in order to reduce numerical error. In the same way, the velocity is ramped down to zero at the end of simulation. This option changed the energy output in some ways, though not giving an overall improvement of the balance. This was no surprise seeing as the energy output was unreasonable during the whole analysis, and mostly after 3-4 seconds. The introduction of a smooth step amplitude should provide most change in the energy at the very start and end.

Energy dissipating effects may occur when one forces the structure to move passed an obstacle in a constant velocity regardless of the resistance. A way of avoiding this is to introduce the velocity as an *initial velocity* in the initial step. The problem with this is first of all that the velocity needs to be applied *before* the gravity and buoyancy, which means that there is no time to reach static equilibrium before the puncher hits the ice. In addition, this requires the application of mass to the rigid puncher, giving an acceleration which should not be there seeing as the cylinder in the experiment is held by steel wires. Due to the weak nature and little resistance of the ice rubble, the constant velocity should not be a problem. The cylinder in the experiment supposedly managed to keep an approximately constant velocity even when interacting with the ice, and the assumption of constant velocity in the numerical simulation seems to be valid.

The strange energy output for the first part of the simulation with metal properties may illustrate the effect of a constant velocity. Most likely this is the cause of the large variation of the energies. The much stiffer behaviour of metal will provide a large resistance towards the motion of the puncher, dissipating energy as the puncher is forced to move with constant velocity. This material is an example of when the initial velocity should be used in stead.

4.5 Mesh Dependency

The transition from a pizza slice geometry to a cubic geometry of the Eulerian domain only affected the analysis run-time, making the analysis run faster for the regular cubic domain due to more regular elements. This in spite of having a larger amount of elements. The stable time increment is calculated from the smallest element size, which was much smaller for the more irregular mesh.

In order to calculate the contact forces, the mesh in the slave structure (in this case the ice/Eulerian domain) should be denser than the mesh in the master structure (the puncher) – at least in the contact zone. A new model was made by creating a denser mesh in the contact zone of the cylinder and the ice: First for a small area, second with the dense mesh reaching the bottom of the domain. The rest of the domain had a coarser mesh in order to reduce the calculation time. The first mesh gave bad and unlikely results for both the energy and the reaction force. The reaction force did not seem reasonable and the energies increased excessively. Although having defined a dense mesh in the contact zone, the material still moved beneath this zone, reaching the coarse mesh. To be able to track the material boundaries, the mesh needs to be sufficiently dense in the regions the material is expected to relocate to. Dassault Systémes (2012*a*) states that for Coupled Eulerian-Lagrangian analyses, a simple, regular grid of Eulerian elements often yields the best accuracy, and that it is unnecessary creating a conforming mesh. This is because the contact algorithm automatically computes and tracks the interface between the Lagrangian structure and the Eulerian material. The definition of a small contact zone created irregular shaped elements in the transition zone between the different regions, which is probably the reason for the erroneous results.

When increasing the dense mesh region to reach the bottom of the Eulerian domain, as in test 17, irregular shaped elements were avoided. The final adapted mesh showed better energy values than the regular mesh. Even though the penalty work still was too high, the external work was closer to the internal work and no longer smaller than the penalty work. The reaction force also seemed reasonable. When visualizing the material deformation, however, it became obvious that the material boundaries was not as well defined as for the previously used, regular mesh. This is illustrated in figure 4.3, for the final adapted mesh, representing test 17 in Appendix A. This proves that this particular problem is very mesh sensitive and the results are dependent upon regular elements as well as a sufficiently dense mesh in the region of material deformation.

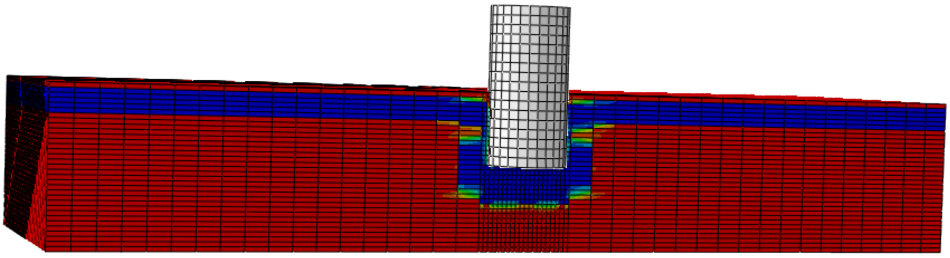

Figure 4.3: *Material deformation, test 17*

4.6 Contact Definition

One of the main problems with the energy balance is the large penalty work, arising from the contact forces. Therefore it was desirable to check the influence of different input options for the contact definition. Some of the tested remedies have been to introduce contact damping, but this only improved the viscous dissipation, and defining pure master-slave surface weighting, giving the exact same results.

The penalty stiffness has been altered by varying the penalty stiffness scaling factor between 0.01 and 5. If the reason for the imbalance in energy is the penalty stiffness, the question is whether the error lies in the accuracy or if this is a numerical error.

The change of penalty stiffness had a major effect on the energy. At first, the penalty stiffness was increased by a factor of 5. This gave a much larger penalty work, and suggests that the problem is not with the accuracy - in which case the penalty solution should be improved. The next step was to reduce the penalty stiffness to account for the possibility of numerical errors from too large penalty numbers. The reduction of penalty stiffness reduced both penalty work, artificial strain energy and viscous dissipation. As a consequence, the external work was increased to reach about the same level as the internal energy. With a penalty scale factor of 0.01, the external work and internal energy was approximately in equilibrium and the artificial strain energy was reduced to an acceptable value of 2 % of the internal energy. As can be seen from figure 4.4, the energy output, represented by the penalty work, changes significantly between scaling factors 5-0.1, but the difference between 0.1 and 0.01 is minimal.

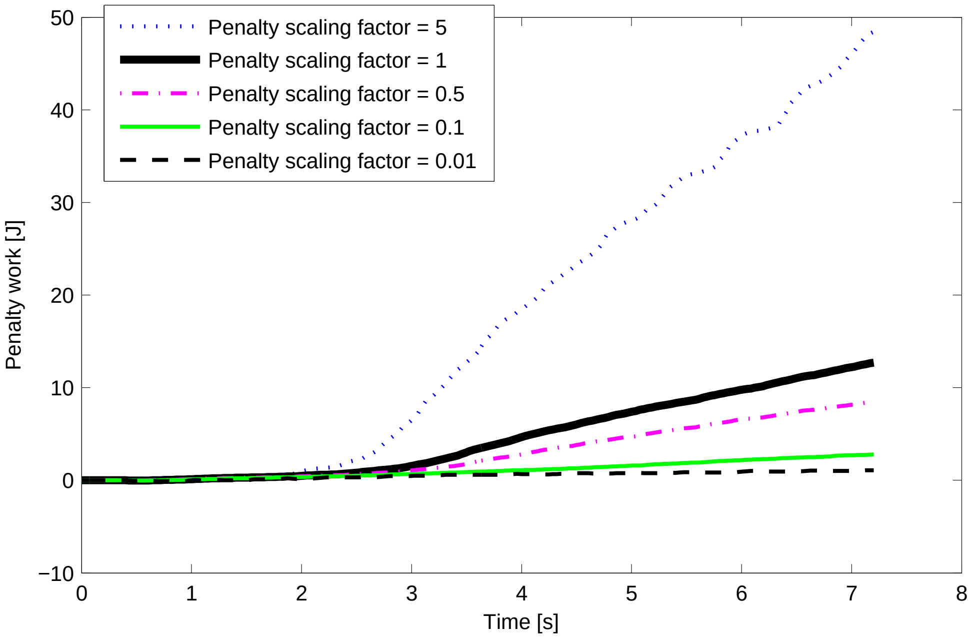

Figure 4.4: *Change of penalty work for scaling factor between 5 and 0.01*

The total energy output showed that the total energy was better for a penalty scale factor of 0.1 than 0.01, though the difference is minimal. The kinetic energy also showed a different pattern for the smallest scale factor than for the others. The external work was higher for a scale factor of 0.1 than 0.01, and for the latter, the external work became slightly larger than the internal energy. This might indicate that the smallest scale factor is starting to produce a reduced accuracy.

Ştefancu et al. (2011) did a study on the influence of input parameters for the penalty method. Although using the Finite Element software Ansys, they came to the conclusion that reducing the tangential penalty stiffness (varying it between 1 and 0.01) only affected the analysis run-time. The energy output was not affected. In contrast to this analysis, they used metal properties. It might be that such numerical software produces better accuracy for stiffer and more common materials. The penalty stiffness is supposed to be calculated on the basis of the stiffness of the underlying materials, but it might be that this is overestimated for soft materials, causing numerical error. When reducing the value of the elastic modulus from the metal simulations to a value of 210 MPa, the analysis is able to run faster. The results show that the internal energy and external work is in balance. The penalty work is small compared to the other energies, despite basically no plastic strains, which enhances the theory last mentioned.

Despite the improvement of the energy balance, the reaction force plots for the different tests show that for penalty scale factors from 1 down to 0.01 the reaction force is actually not that different. Except from individual peaks, the reaction force actually shows the same trend and would give approximately the same results if the plots were smoothed. The imbalance in the energy affects the solution only locally. A larger maximum force is seen in the simulation with scale factor equal to 0.01, which may again emphasize the possibility of reduced accuracy. A larger effect on the reaction force is seen when *increasing* the penalty stiffness from the default value, where the solution shows large oscillations towards the end.

4.7 Geometry

After advise from Håkan Lind, application engineer at SIMULIA Nordics CSE (Abaqus technical support), one should try to avoid sharp corners in the structure interacting with the Eulerian material. This was done by introducing a fillet to the bottom corner of the structure (test 29). Rounding off the bottom edge of the puncher gives a huge improvement of the energy balance - especially with regards to the artificial strain energy which is now reduced to 1.4 % of the internal energy at the end of simulation. The energy, given in figure 4.5, is almost in equilibrium, although the external work and internal energy is not entirely equal.

Comparing the simulation run with a round corner to the simulations with penalty scaling, the first gives slightly better results. The artificial strain energy is less and the penalty work is about the same order - giving a more constant total energy. To be able to reduce the penalty work even further the best solution would probably be to combine a rounded corner with a slight reduction of the penalty stiffness - and perhaps in combination with the adapted mesh from test 17 (section 4.5).

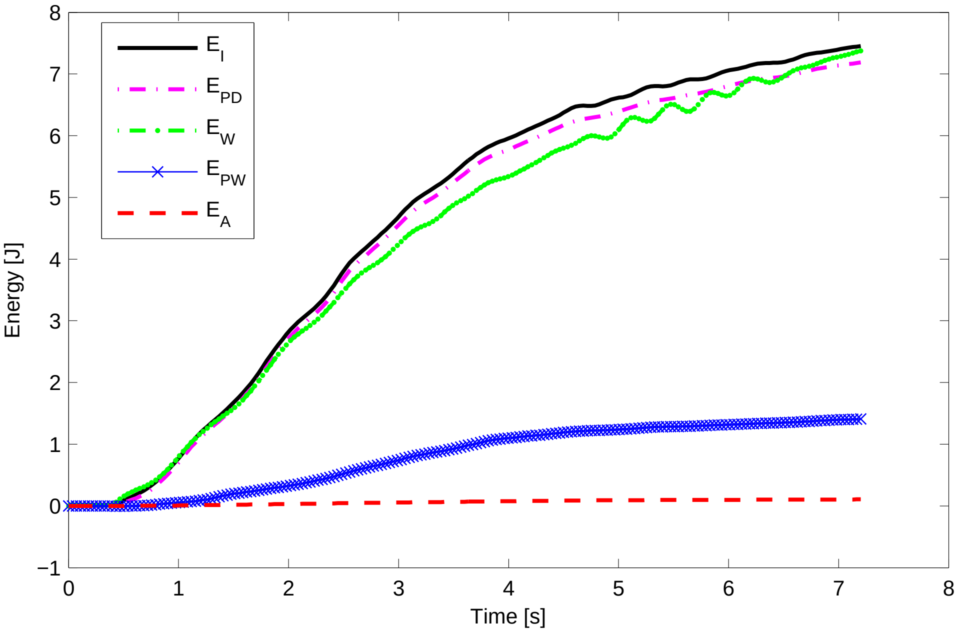

Figure 4.5: *Energy balance for test 29 - fillet on bottom edge*

5 Finite Element Models

The experiments are modelled in the Finite Element software Abaqus, version 6.12, using explicit analysis. Both cases are modelled using the Coupled Eulerian-Lagrangian approach (section 2.4.3), which copes with the challenge of large displacements of the ice rubble as well as the interface between the puncher and the ridge.

To give a best possible foundation for a comparison, the full scale and model scale cases are modelled in the same way, changing only the material parameters, the geometrical sizes and the loading velocity.

5.1 Assumptions Behind the Models

The following assumptions for the Finite Element model are made:

- The temperature throughout the ice rubble is assumed constant
- The ice rubble is assumed homogeneous, i.e material parameters are considered constant over the volume
- The geometry is simplified to be axisymmetric, i.e the thickness is considered constant
- The movement of the puncher is assumed purely vertical

5.2 Geometry and Mesh

Puncher
The test rig in the full scale measurements is simplified as a loading plate on top of the consolidated layer. The same is used for the model scale simulations. The plate is modelled as a discrete rigid part with diameter according to table 3.2 for the full scale simulations, and constantly equal to 0.7 m for the model scale simulations. The mesh is composed of rigid elements R3D4. Sharp corners at the bottom edge is avoided using a fillet with radius equal to the size of the nearest Euler elements, see section 4.7.

Euler domain
The Euler mesh consists of four parts:

1. Void elements at the top

2. A Lagrangian consolidated layer with an elastic material definition *inside* the upper void region
3. Ice rubble, described using the Modified Cam Clay material model
4. Void elements at the bottom

Figure 5.1 shows a sketch of the numerical model with the four different regions. The grey areas represent void. As illustrated in the figure, a cut is modelled through the consolidated layer, as was done in the experiments. To avoid irregular elements, the cut is made as a square around the circumference of the plate in stead of a circle.

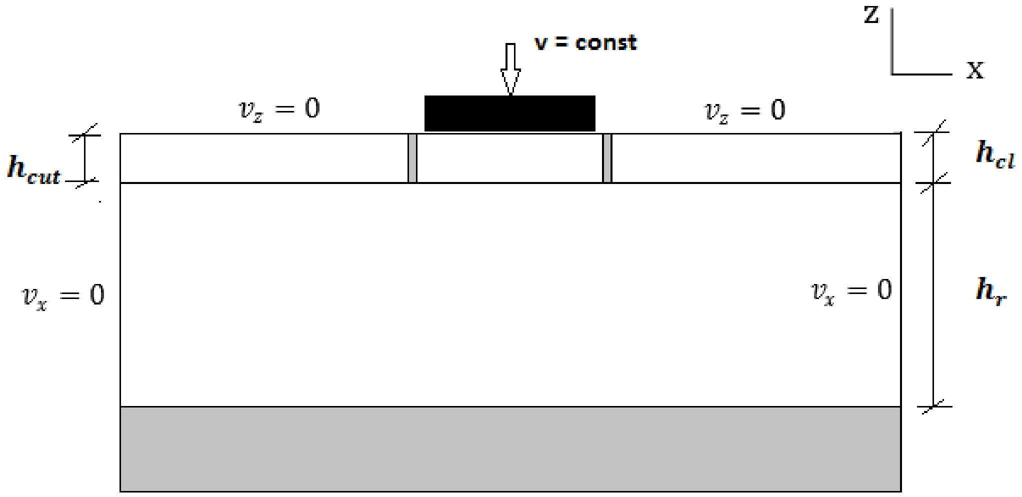

Figure 5.1: *Planar sketch of the numerical model, defining the rubble depth (h_r), the consolidated layer thickness (h_cl) and the cut depth (h_cut).*

Seeing as the ice properties are assumed homogeneous and the depth constant, only half of the ice ridge is modelled, utilizing the axisymmetry while retaining the 3D effects.

The Eulerian domain consists of EC3D8R reduced integrated elements, which are the only elements available for Eulerian analyses. The elements are of second order accuracy with stiffness based hourglass control (see section 4.2). The mesh is made denser in the area beneath the puncher, where most of the material movement is expected. Figure 5.2 shows the geometry and mesh of the numerical model in Abaqus. The grey objects are Lagrangian parts - topmost, the puncher and beneath, the two parts of the consolidated layer.

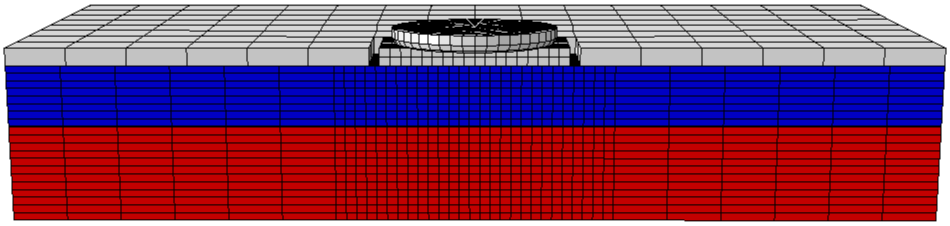

Figure 5.2: *Numerical model in Abaqus - geometry and mesh*

The blue region represents the initial material location of the rubble, while the red region at the bottom represents void.

5.3 Material

The consolidated layer is modelled as an elastic layer. The density is equal to the ice densities from tables 3.1 and 3.2. The elastic modulus is different for model scale and full scale measurements. It is set to be 1 GPa in the full scale simulations. For the model scale tests, an initial elastic modulus of 17.1 MPa is defined, taken from Liferov et al. (2003). Poissons ratio is chosen to be 0.3 for both the consolidated layer and the ice rubble, which is common for granular materials.

The ice rubble is modelled with the critical state (clay) plasticity model from the Abaqus material library. Setting the wet yield surface size, β, and the flow stress ratio, K, equal to 1, this becomes the Modified cam clay model. The resulting input required for this model is the stress ratio M and initial volumetric plastic strain $\varepsilon^{p}_{p,0}$. The latter is set to zero, whereas the stress ratio is to be estimated from the simulations. Serré (2011) did pile tests on ice rubble and found the Mohr-Coulomb frictional angle to be 45, corresponding to a stress ratio M of 1.85. He later argued that the angle more likely could vary from 30 to 45 degrees, and he states that this was also found by Liferov et. al (2003). A stress ratio ranging from 1.3-1.85 is therefore studied in the following.

In the full scale tests, Heinonen (2004) states that the elastic modulus varied from 22-120 MPa for the ice rubble, the smallest values originating from tests done in year 2000. An initial value of E=100 MPa is therefore chosen. The initial value of the elastic modulus for the model scale simulations is set to 1.1 MPa, as was done by Liferov et al. (2003).

Using Abaqus/Explicit, a piecewise linear hardening law must be defined, where the yield stress in hydrostatic compression, p, is related to the corresponding plastic volumetric strain, ε_p^p. The hardening curve was calculated in Matlab, using the hardening rule from equation (2.13), rearranged to get the pressure as in equation (5.1). κ was originally set to 0.03, as was estimated by Heinonen (2004) for full scale ice ridges. Both κ and λ was later varied to examine the effect of the difference $(\lambda - \kappa)$.

$$p_{i+1} = (\lambda - \kappa) \cdot \frac{p_i}{\lambda - \kappa - \nu_{i+1} \cdot \Delta\varepsilon_p^p} \tag{5.1}$$

ν_{i+1} is calculated as in equation (5.2), where the initial specific volume in equation (5.3) is defined by the porosity η of the ridges.

$$\nu_{i+1} = \frac{\nu_i}{\Delta\varepsilon_p^p + 1} \tag{5.2}$$

$$\nu_i = \frac{1}{1 - \eta} \tag{5.3}$$

The ice rubble is modelled by prescribing an initial material location with depth equal to the given rubble depth from tables 3.1 and 3.2. The depth of the consolidated layer is for full scale simulations assumed to be the depth of the cut in lack of more precise measurements. For the model scale tests, the thickness measurements of the consolidated layer indicate that the consolidated layer is thinner than the cut. The mid-value of the thickness intervals has been used.

When modeling two materials in the same Euler mesh, the Eulerian-to-Eulerian contact is sticky. This means that Eulerian materials do not mix, and that relative motion between the two materials in the same element is not allowed (Dassault Systémes, n.d.). This causes the consolidated layer to follow the ice rubble as it is pushed downwards by the loading plate and hence a uniform displacement along the length of the ice rubble. Because of this, the consolidated layer needed to be modelled using Lagrangian elements, which gives the possibility of defining a more complex contact. The Lagrangian consolidated layer is modelled *inside* the Eulerian mesh, as in figure 5.1.

5.4 Loads and Boundary Conditions

Since the consolidated layer is modelled as a Lagrangian structure, it becomes more complicated modelling a load that changes above and below the waterline, as was done by Nilsen (2014). For simplicity, it is assumed that the whole consolidated layer lies above the waterline. The ice rubble in the numerical model is subjected to buoyancy forces, modelled as an upward gravity using equation (5.4). The density of the ice rubble is defined in equation (5.5). To ensure static equilibrium, the buoyancy force is balanced by a pressure applied to the surface of the consolidated layer. Equation (5.6) gives the value of the pressure, modified to account for the void region that is the area of the cut.

$$b = (\frac{\rho_w}{\rho_r} - 1) \cdot g \tag{5.4}$$

$$\rho_r = \eta \cdot \rho_w + (1 - \eta) \cdot \rho_{ice} \tag{5.5}$$

$$p = b \cdot \rho_r \cdot h_r \cdot \frac{A}{A - A_{cut}} \tag{5.6}$$

where

ρ_{ice}	is the density of ice
ρ_w	is the density of water
η	is the porosity of the ice rubble
g	is the acceleration of gravity
A and A_{cut}	is the area of the consolidated layer and cut, respectively
h_r	is the thickness of the ice rubble, $h_r = h_k - h_{cl}$

Symmetry boundary conditions are assigned to the symmetry plane, while all other vertical planes are constrained from movement in the normal direction. This is done to prevent material from flowing in or out of the edges of the domain, which will generally happen without constraints when the elements on the boundary contain material (Dassault Systémes, n.d.). The consolidated layer surrounding the cut is prevented from moving vertically. The boundary conditions in the xz-plane are illustrated in figure 5.1.

In the full scale measurements, no constant velocity was gained in the lowering of the loading plate. The system is hydraulic, and a constant velocity is hard to retain, especially when the system approaches its capacity. Plots of the measured displacements from the experiments have been used to try and recapture the general motion of the cylinder by simplifying the displacement as two linear functions. The external loading is applied by prescribing a constant velocity with two different amplitudes corresponding to the displacement functions.

For the model scale simulations the external loading is applied as a constant velocity corresponding to the displacement graphs of figures 3.6 and 3.7, lowering and lifting the plate over four different steps.

5.5 Contact

The contact is modelled using the general contact definition. A penalty friction formulation is used for contact between the consolidated layer and the ice rubble. An ice-ice friction coefficient of 0.1 is used, collected from Serré (2011). The contact between the puncher and the middle part of the consolidated layer is defined as hard.

6 Numerical Analysis

In the following, the results from the numerical simulations will be presented; first for the model scale tests and second for the full scale tests. A parameter study was conducted to fit the experimental results as closely as possible. The following parameters were studied: Hardening parameters λ and κ, initial pressure p_0, stress ratio M and Young's modulus E.

For both simulations, the deformation mode, results from parameter study and final results are presented. For the model scale simulations, the effect of the interpretation of the geometry has also been investigated. Since the full scale experiments are performed using a much more complicated loading system and the ridges are not loaded in a constant velocity, the effect of the loading velocity on the results has been examined.

6.1 Model Scale

Since the buoyancy from the consolidated layer is excluded in the numerical simulations, this has been calculated from equation (6.1) and added to the numerical results.

$$\begin{aligned} B_{cl} &= (\rho_w - \rho_{ice}) \cdot g \cdot A \cdot u \quad \text{for} \quad u < h_{cl} \\ B_{cl} &= (\rho_w - \rho_{ice}) \cdot g \cdot A \cdot h_{cl} \quad \text{for} \quad u \geq h_{cl} \end{aligned} \tag{6.1}$$

u is the displacement of the loading plate into the rubble, with a maximum value equal to the thickness of the consolidated layer.

6.1.1 Deformation Mode

In the laboratory experiments, the loading is comprised of two load steps. When the plate is lifted after the first load step, the ice follows, floating up to the water surface again. The ridge is thereafter reloaded in the same manner.

In the numerical simulations, plastic strains in the first load step causes permanent deformations in the ice rubble, and the buoyancy alone is too small to give reversed deformation. The rubble remains in the deformed state when the plate is lifted, as is shown in figure 6.1. The maximum principle plastic strains at the end of the first load step is in the order of 20-30 %.

Since the plastic deformation precludes the utilization of a second load step, the focus has been on recapturing the magnitude and shape of the first peak.

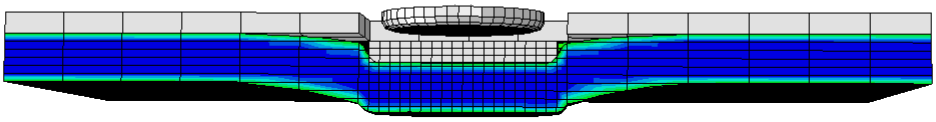

Figure 6.1: *Example of deformation subsequent to the first load step (test 10, ridge 3002)*

Figures 6.2a and 6.2b show the plastic strains and shear stresses at the end of the first load step for ridge 3001. The plastic strains in figure 6.2a is the maximum principle plastic strains, which are mainly caused by plastic *shear* strains for these simulations. Both figures indicate the same shear surface as in the principle sketch of the punch test in figure 3.9.

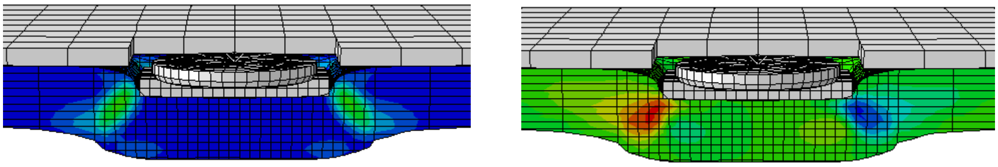

(a) *Maximum principle plastic strain* **(b)** *Shear stress, S_{23}*

Figure 6.2: *Plastic strain and shear stress for ridge 3001, test 15*

By requesting output for the integrated volume of the Eulerian material, the volumetric strains could be calculated. For ridge 3001 and 3002 the total plastic volumetric strains were 1.9 % and 1.7 %, respectively.

For all of the following plots for model scale simulations, the reaction force is plotted against time. Due to the constant velocity of the loading plate, the development of the reaction force will be the same as if plotted against displacement.

6.1.2 Effect of Geometry Interpretation

The consolidated layer thickness is given as an interval, measured by thermistor strings. Since there is no way of knowing the exact value, the effect of the consolidated layer thickness on the reaction force has been studied. Figure 6.3 shows the reaction force for two numerical simulations on ridge 3001. The only difference between the two cases is the thickness of the consolidated layer. The maximum force differs with about 25 N for a thickness difference of 30 mm, the highest value originating from the thinnest consolidated layer. The difference decreases from the time of which the thinnest consolidated layer is totally submerged.

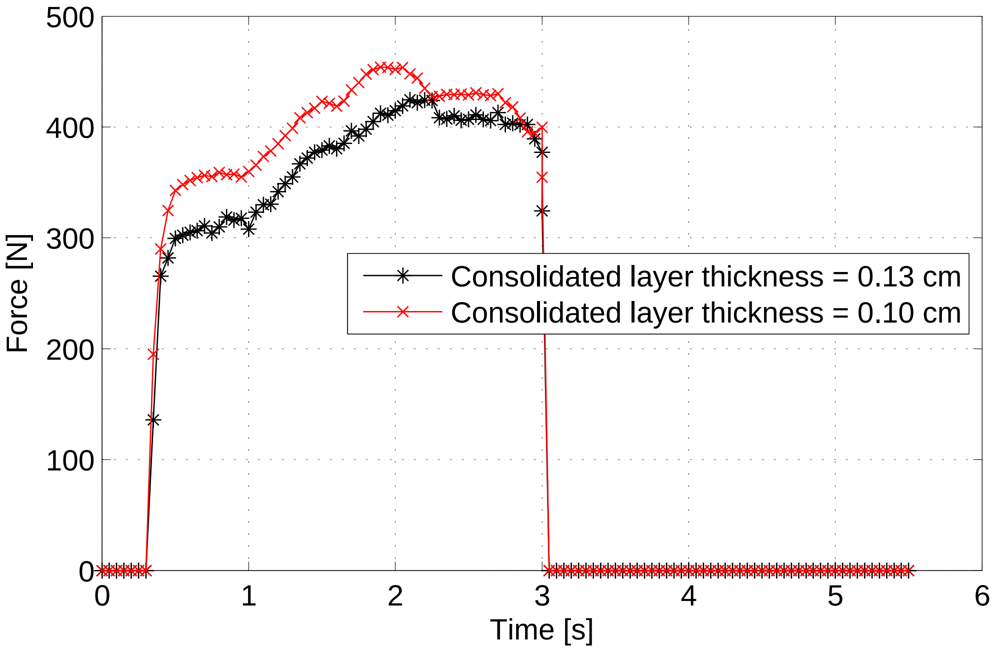

Figure 6.3: *Comparison of results for different thickness of the consolidated layer of ridge 3001*

For ridge 3002, the depth is announced to be 700 mm. The cross section of the ridge (figure 3.5), however, shows a thickness closer to 400 mm. The same goes for the cross sections taken at port side and starboard side (not included in this paper). Figure 6.4 gives the reaction force for two simulations with the same material parameters, but with a keel depth varying from h_k=0.7 m to h_k=0.4 m. For a difference in keel depth of 0.3 m, the reaction force differs with between 400 and 600 N. As can be seen from the figure, the reaction force is more than doubled for the deepest keel. The small peak in the beginning of the time interval for the deepest keel is due to the constant velocity of the plate, and could have been avoided by applying a smooth step amplitude.

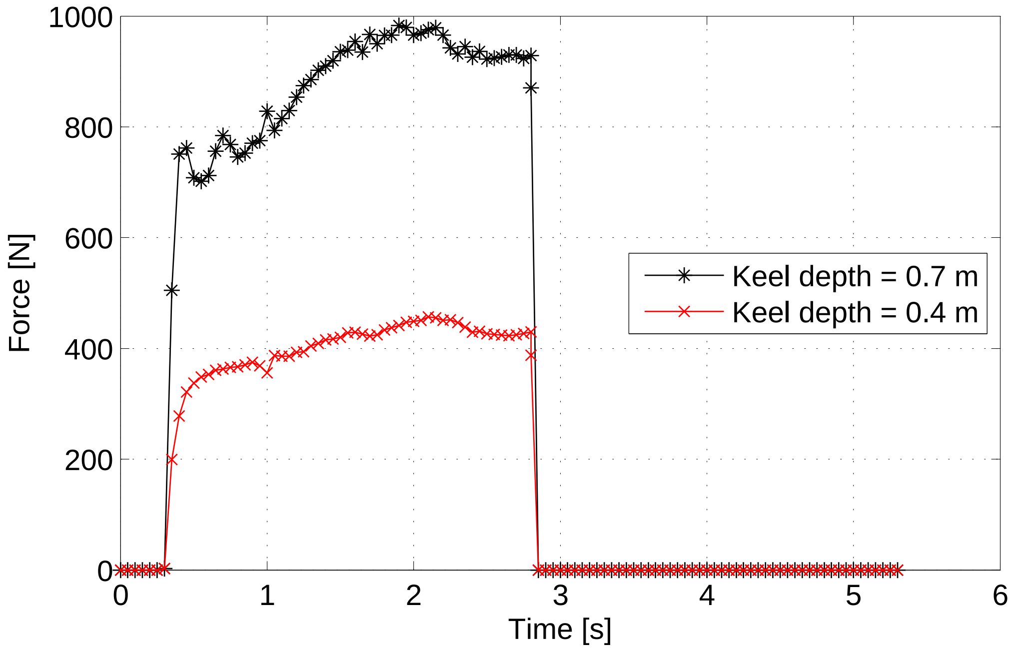

Figure 6.4: *Comparison of results for different keel depths of ridge 3002*

Ridge 3001 is stated to be 400 mm deep. However, based on the cross sectional plots of the ridge, it seems to be deeper than ridge 3002. Simulations have therefore been performed using both:

1. A keel depth of 0.4 m along with a consolidated layer thickness of 0.13 m (assumed depth of the cut)
2. A keel depth of 0.45 m along with a consolidated layer thickness of 0.1 m (mid-value of thickness interval)

In order to gain the same reaction force, case 1 requires an initial pressure of 1500 Pa and a stress ratio M of 1.85. For case 2, the initial pressure can be reduced to 1000 Pa and the stress ratio to 1.8. κ and λ are the same for both cases. For a difference in rubble depth of 0.08 m between case 1 and 2 ($h_r = h_k - h_{cl}$), the parameters are quite different.

6.1.3 Parameter Study

For a change in elastic modulus E between 0.9 and 1.1 MPa, the results are almost the same. Variations in κ and λ makes little difference on the results, besides introducing oscillations (possibly numerical noise) for very small differences $(\lambda - \kappa)$.

Figure 6.5 shows the reaction forces from ridge 3001 for different values of initial pressure. The reaction force increases for increasing initial pressure. The increase in stress ratio from 1.3 to 1.85 on ridge 3002, figure 6.6, gives a similar increase in reaction force. The difference is that the latter does not seem to change the shape of the curve, whereas the change in initial pressure influences the hardening.

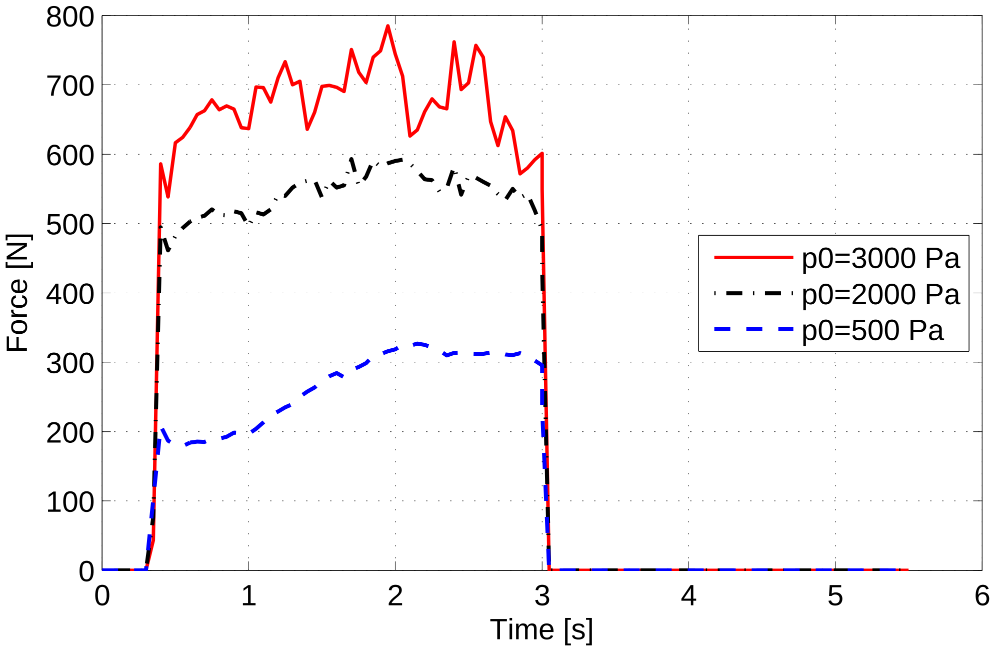

Figure 6.5: *Variation of initial pressure from 500 to 3000 Pa for ridge 3001 (M=1.3)*

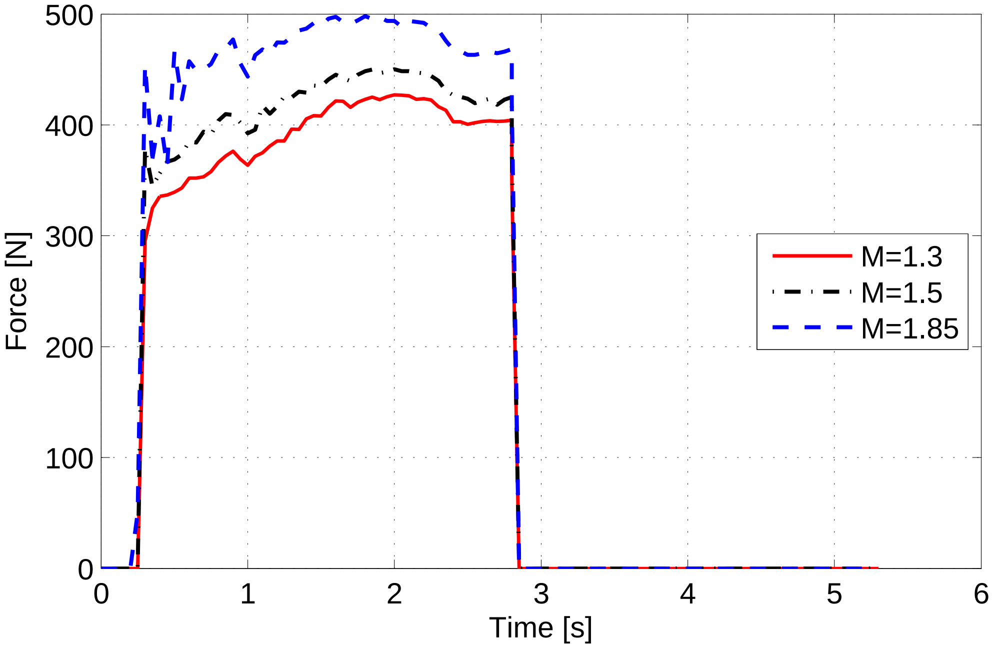

Figure 6.6: *Variation of stress ratio from 1.3 to 1.85 for ridge 3002 (p_0=500 Pa)*

6.1.4 Final Results

The material parameters giving the most similar forces and force development to the experimental results are given in table 6.1. The depths of the keel and consolidated layer is included since these values diverge from table 3.1. Figures 6.7 and 6.8 give the final reaction force from the numerical simulations on ridge 3001 and 3002, compared with the experimental results of test 3001CL and 3002CL. $(\lambda - \kappa)$ is smaller for ridge 3002 due to the earlier hardening of the material in this test.

Test #	3001CL	3002CL
κ	0.01	0.03
λ	0.15	0.13
$\lambda - \kappa$	0.14	0.1
p_0 [Pa]	1000	500
$\mu_{ice-ice}$	0.1	0.1
E_{rubble} [MPa]	1.1	1.1
M	1.8	1.8
h_k [m]	0.45	0.40
h_{cl} [m]	0.1	0.12

Table 6.1: *Final properties for numerical simulations of model scale tests*

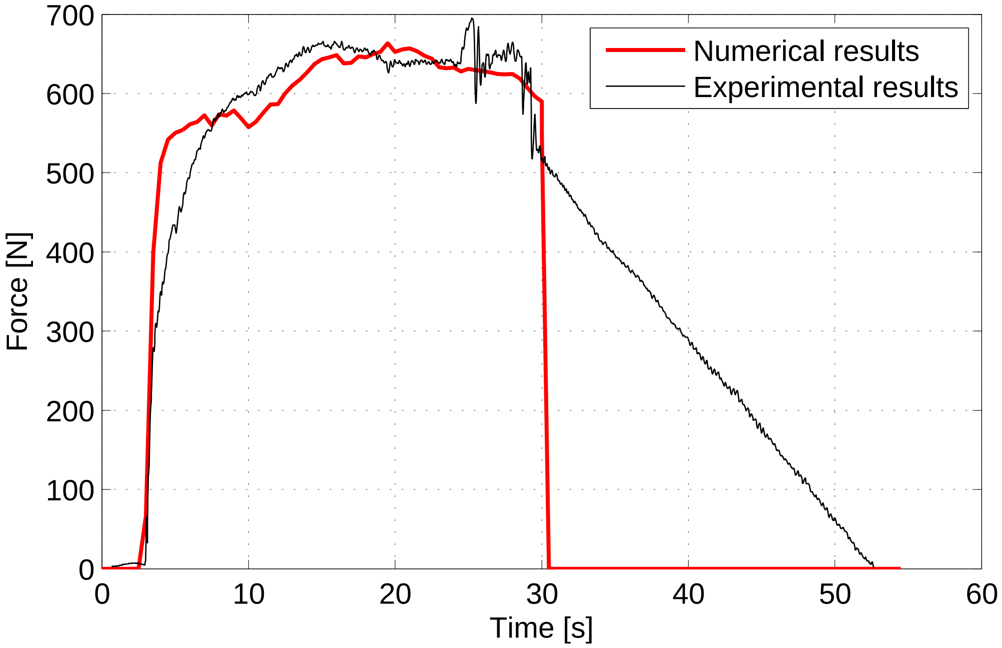

Figure 6.7: *Numerical vs. experimental results for test 3001CL. Parameters* p_0*=1000 Pa, M=1.8,* $\lambda - \kappa$*=0.14*

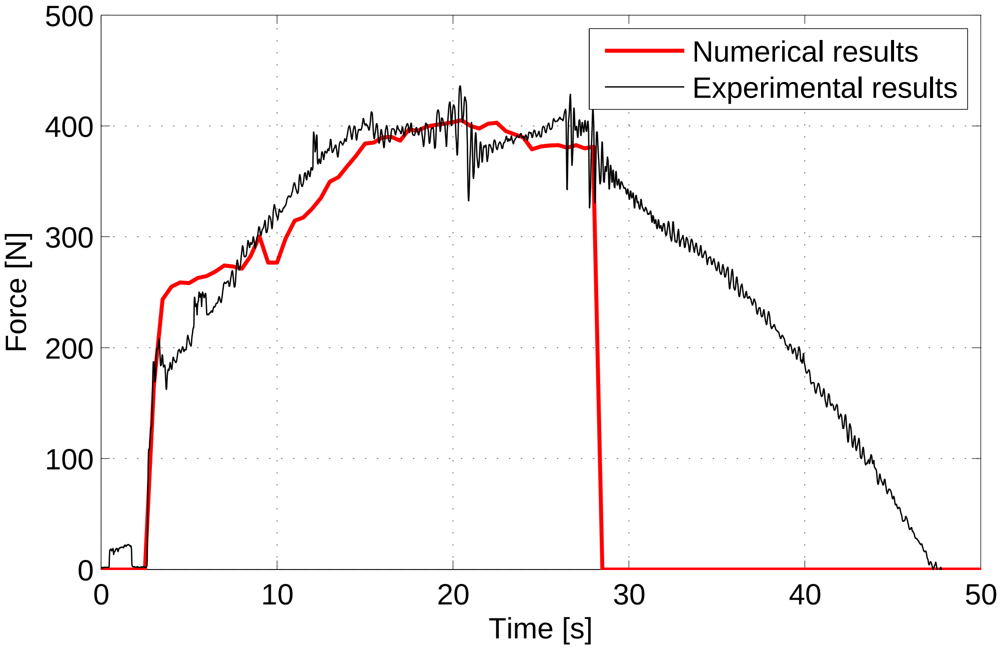

Figure 6.8: *Numerical vs. experimental results for test 3002CL. Parameters* p_0*=500 Pa, M=1.8,* $\lambda - \kappa$*=0.1*

6.2 Full Scale

In the numerical simulations, buoyancy from the consolidated layer is not accounted for. The middle part of the consolidated layer - inside the cut - will give a contribution to the reaction force when it is pushed below the water line. This contribution, however, only accounts for about 2 kN at the time of peak force, and is hence neglected. The buoyancy from the water on the plate is also excluded in the simulations, but since the total displacement is so small, the plate will barely reach the water line and give a negligible contribution compared to the large total load.

6.2.1 Deformation Mode

Figures 6.9a and 6.9b give the deformation of the rubble for full scale test 2, along with the plastic strains and shear stress, respectively. The maximum principle plastic strains are in the order of 10-15 % when the movement is stopped, though much lower for test 10, where the they are closer to 2 %. The change in volume of the ice rubble throughout the analysis has been calculated, giving the total volumetric plastic strain given in table 6.2. The volumetric strain for test 6 is not reliable since the initial pressure was increased to an unrealistic value, as will be explained later.

Test #	2	6*	9	10
Plastic volumetric strain [%]	0.57	0.045	0.27	0.51

*high initial pressure gives little expansion

Table 6.2: *Volumetric strain in full scale tests*

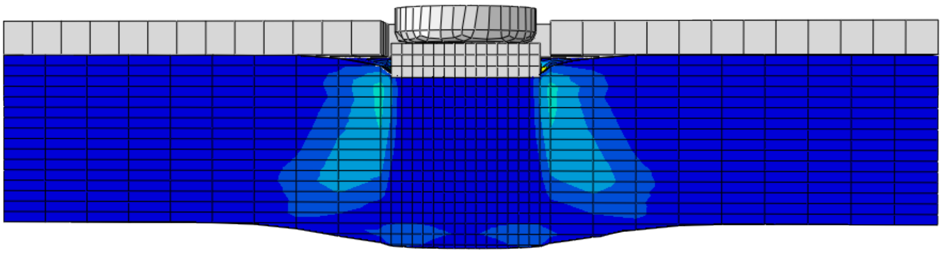

(a) *Maximum principle plastic strain*

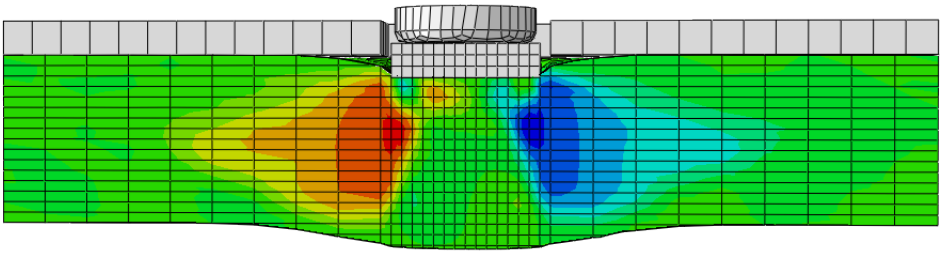

(b) *Shear stress, S_{23}*

Figure 6.9: *Rubble deformation, along with plastic strain and shear stress for test 2, full scale*

6.2.2 Applying External Load

The reaction force proved to be dependent on the applied loading velocity. From the displacement measurements in the field data, figures 3.10 through 3.13, it is evident that a constant velocity was not achieved. Figure 6.10 shows an example of the influence of loading velocity for full scale test 2. The reaction force on the loading plate is plotted against the displacement of the plate. The dashed line represents the reaction force for a simulation with a constant loading velocity equal to 31 mm/s. The solid line represents the reaction force for a simulation run with a velocity varying from 2.6 mm/s to 25 mm/s. The corresponding displacement for the latter case is shown in figure 6.11. The parameters used for the high speed simulation are p_0=20 kPa and M=1.7. To reach the same maximum value of the reaction force in case 2, the parameters need to be increased to p_0=24 kPa and M=1.85. The change in material parameters does not change the shape of the curve, it only increases the value of the reaction force.

The following is observed in the comparison:

1. Higher velocity produces a larger reaction force
2. Higher velocity gives a larger load drop
3. The higher velocity shows a linear increase until maximum load, whereas the stiffness changes for a low initial velocity

The larger reaction force for the high speed simulation is due to the acceleration of the ice rubble that occurs for a rapid loading.

For the remainder of the simulations, the velocity has been applied according to the displacement development of figure 6.11, since this is more similar to the actual loading in the experiments. The velocities have been calculated by approximating the displacements of figures 3.10 through 3.13 as two linear curves, resulting in two amplitudes for the velocity.

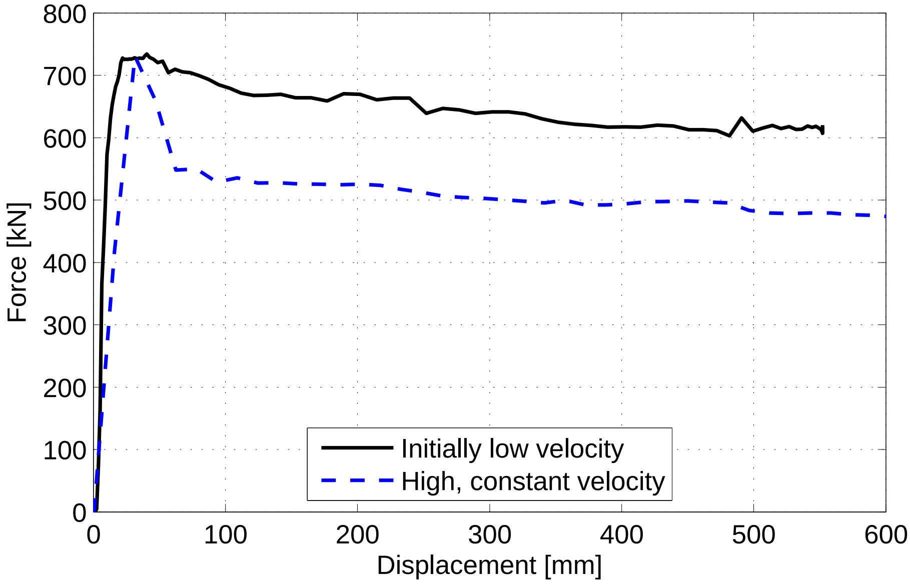

Figure 6.10: *Example of the influence of loading velocity for full scale test 2. Case 1) has a constant velocity of v=31 mm/s with p_0=20 kPa and M=1.7, and 2) has an initially low velocity of v=2.6 mm/s, increasing to 25 mm/s with p_0=24 kPa and M=1.85*

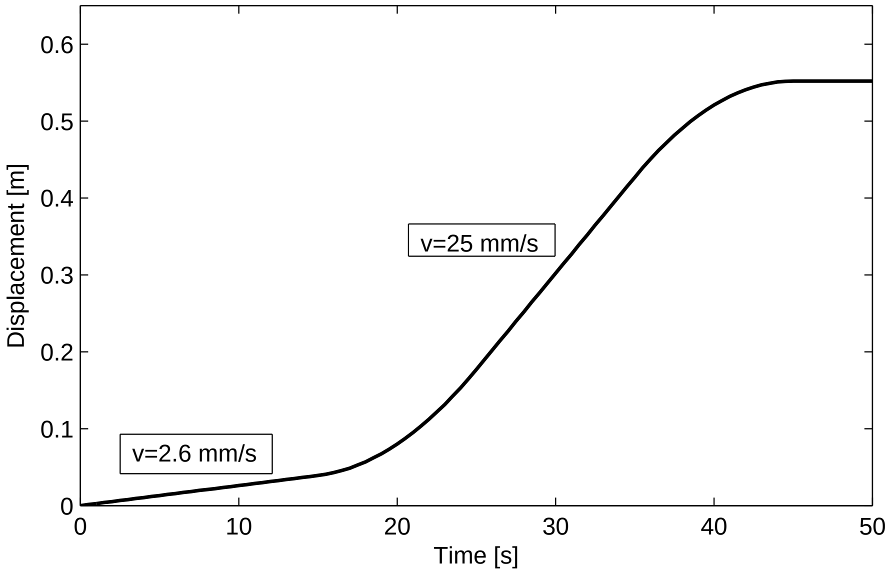

Figure 6.11: *Displacement of the plate for full scale test 2. The applied velocity is varying from v=2.6 mm/s to v=25 mm/s*

6.2.3 Parameter Study

Varying the value of Young's modulus does not change the value of the reaction force, apart from a small change in the initial stiffness for a variation of E-modulus between 50 and 120 MPa. For the rest of the simulations, Young's modulus is chosen to be 100 MPa. An increase in stress ratio M gives a uniform increase in reaction force, meaning that the difference in reaction force between two tests with different M is the same throughout the simulation. The initial pressure p_0 has the same effect. Higher values of p_0 increases the reaction force, but also increases the residual force.

All simulations showed the same tendency for the reaction plot. Changing the hardening parameters λ and κ did however alter the shape of the peak, making it smoother for smaller values of λ, or a smaller difference between κ and λ.

6.2.4 Final Results

Table 6.3 gives the final input for the four tests. These are the properties that gave the best resemblance to the experimental results. Since the numerical results showed nowhere near enough load decrease after maximum force, the main focus has been on reaching the experimental peak force.

Test #	2	6*	9	10
κ	0.03	0.03	0.03	0.03
λ	0.07	0.07	0.07	0.08
$\lambda - \kappa$	0.04	0.04	0.04	0.05
p_0 [kPa]	24	>50	19	22
$\mu_{ice-ice}$	0.1	0.1	0.1	0.1
E_{rubble} [MPa]	100	100	100	100
M	1.85	1.9	1.85	1.85

*does not reach maximum force

Table 6.3: *Final properties for numerical simulations of full scale tests*

Figures 6.12a through 6.15b give the results for the reaction force from the numerical simulations, compared with the corresponding experimental results, plotted against the displacement of the loading plate. None of the simulated tests managed to recapture the global failure and large load drop after the maximum force, though a small decrease in the reaction force can be seen for large time intervals. The initial stiffness is somewhat higher for the numerical simulations, except in the case of test 6 where the reaction force increases faster for the experimental results than the numerical. Another difference is that the experimental results seem to show an almost linear increase in reaction force until maximum load. In the simulations, the stiffness changes just before reaching maximum load, indicating plastic deformations.

To retrieve the high values of reaction force from the field measurements, a relatively high value of initial pressure is required. This large initial pressure causes the rubble to compact and affects the deformation - going from a more "plug-like" deformation for low values of p_0 to a beam-like bending for high values.

The simulations of test 6 do not reach the maximum force of the experimental results for any material parameters. Figure 6.13a shows the results for the simulation run with an initial pressure of 50 kPa, which is close to reaching the maximum force, but with an unrealistically high initial pressure. The resulting reaction force oscillates due to large material movement even after the motion of the puncher has terminated. The initial stiffness in the numerical results is actually lower than for the experimental results, and the material does not seem to soften for the highest initial pressure. With an initial pressure of less than 30 kPa, the reaction force stabilizes as for the other tests and does not oscillate. However, this value of initial pressure is not even close to reaching the maximum value of the experimental results.

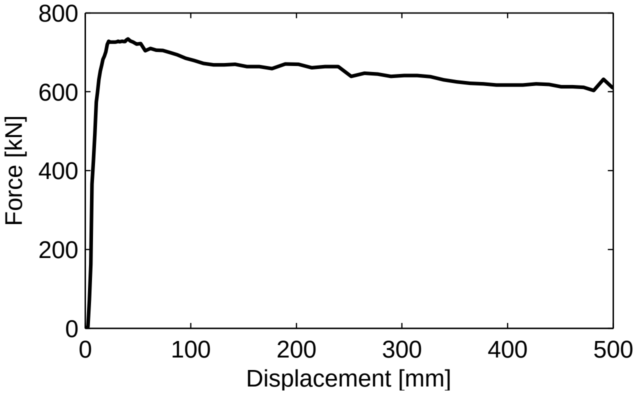

(a) *Numerical results*

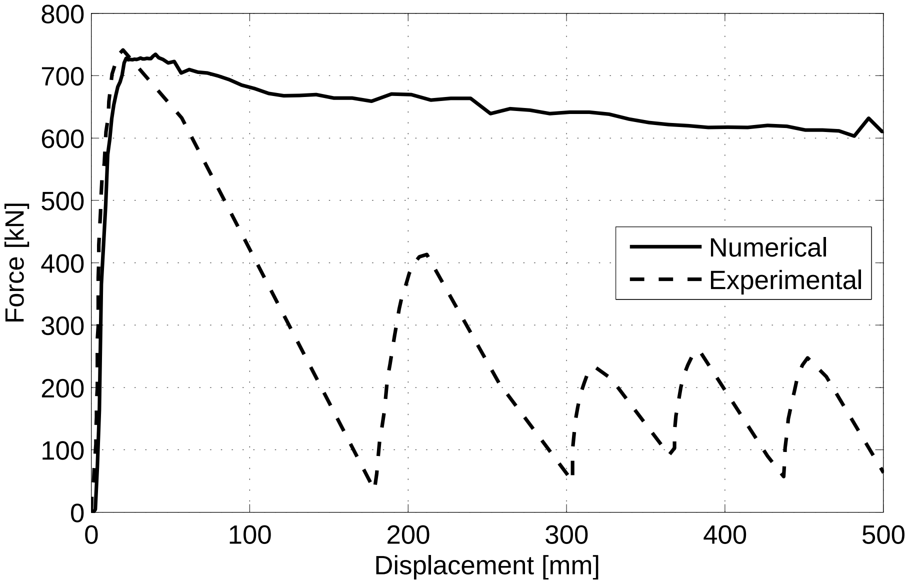

(b) *Numerical vs. experimental results*

Figure 6.12: *Numerical results compared with experimental results for test 2. The x-axis represents the displacement of the plate. Parameters* p_0=*24 kPa, M=1.85,* $\lambda - \kappa$=*0.04*

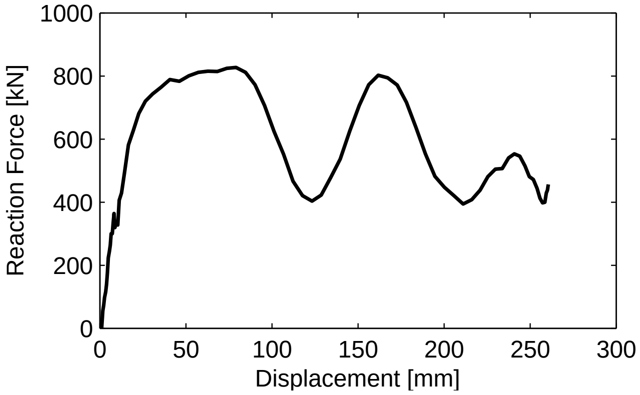

(a) *Numerical results*

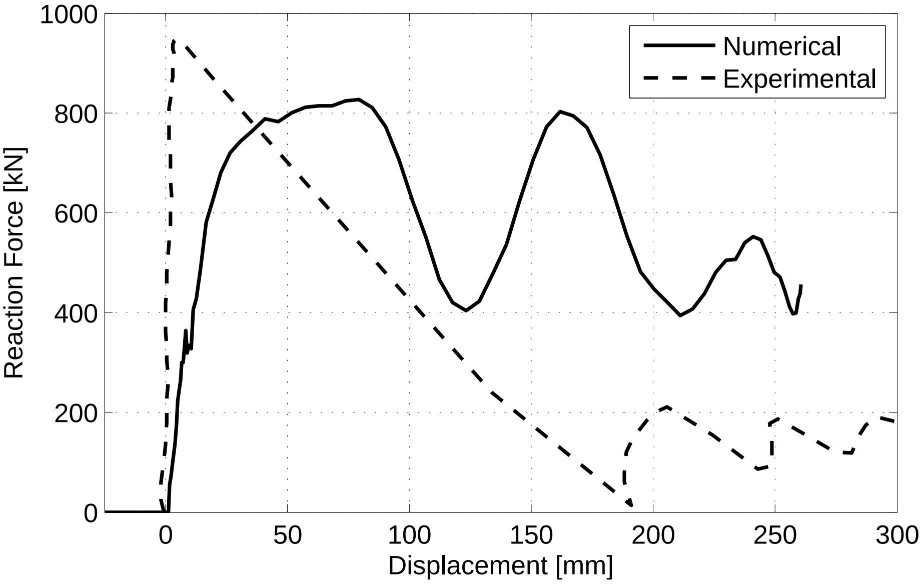

(b) *Numerical vs. experimental results*

Figure 6.13: *Numerical results compared with experimental results for test 6. The x-axis represents the displacement of the plate. Parameters* $p_0 > 50$ *kPa,* $M = 1.9$, $\lambda - \kappa = 0.04$

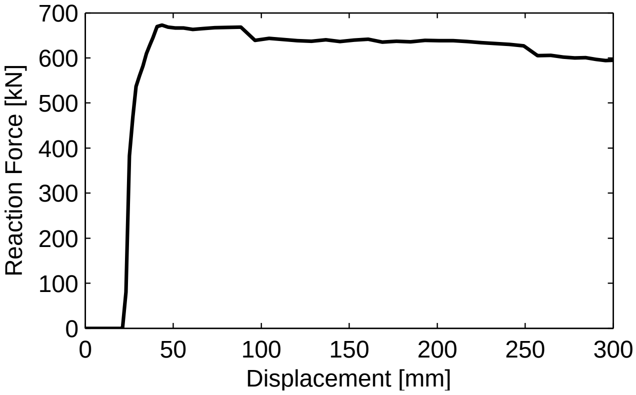

(a) *Numerical results*

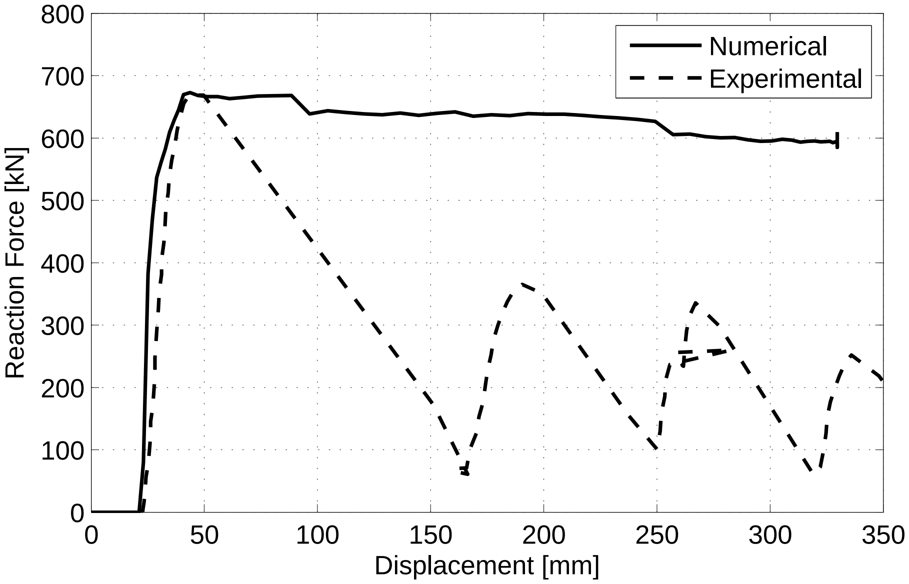

(b) *Numerical vs. experimental results*

Figure 6.14: *Numerical results compared with experimental results for test 9. The x-axis represents the displacement of the plate. Parameters* p_0*=19 kPa, M=1.85,* $\lambda - \kappa$*=0.04*

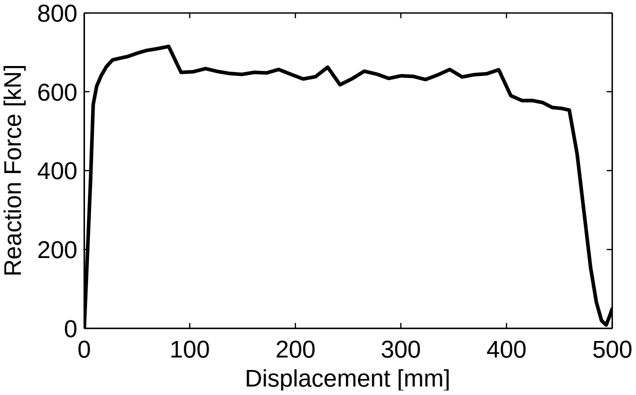

(a) *Numerical results*

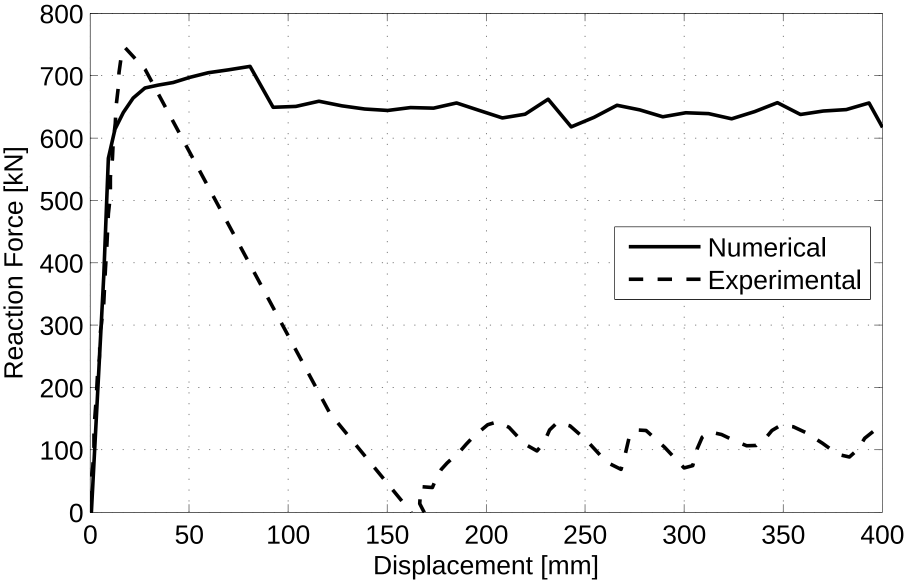

(b) *Numerical vs. experimental results*

Figure 6.15: *Numerical results compared with experimental results for test 10. The x-axis represents the displacement of the plate. Parameters* p_0*=22 kPa,* M*=1.85,* $\lambda - \kappa$*=0.05*

The large load drop at the end of test 10 (figure 6.15a) is due to the termination of the plate movement and is purely numerical.

7 Discussion

7.1 Model Scale Simulations

The numerical simulations provide good resemblance to the experimental results, both in terms of maximum force and force development. A difference is seen in that the material in the experiments seem to start hardening at a slightly earlier stage than the material in the numerical simulations.

In the model scale tests, underwater videos showed that the ice rubble failed in shear after the first load step. The material model does not include a failure criterion - the deviatoric strains (shear strains) are unrestricted in the numerical model and will not cause failure. Heinonen and Høyland (2013) used a shear failure criterion in their user defined material model, which is necessary to simulate the global failure and in this case the upflow of ice when the plate is lifted. The same shear failure zone is, however, seen in the numerical results as the region of high plastic strains and shear stresses from figures 6.2a and 6.2b.

7.1.1 Hardening

The porosity η, initial pressure p_0 and difference $(\lambda - \kappa)$ determines the hardening curve. A small difference between λ and κ gives a faster hardening, but this does not seem to have that much effect for small stresses. The simulations showed that the material experiences more hardening for a small value of initial pressure (p_0=500 Pa), see figure 6.5. This is due to the small stresses occurring in the ice rubble, and the fact that the stress components are easier outside the elastic region for a small p_0 (smaller yield surface). Figure 7.1 illustrates the change in yield surface for a change in initial pressure or stress ratio. It is evident that the hardening is greatly affected by the change in yield surface size. Changing M should theoretically also have an effect on the hardening and softening of the material. In the figure, the increase in M is illustrated by the change in yield surface from the smallest yield surface (black dashed) to the second (blue dashed). Reducing M provides a larger stress range to which softening occurs (η>M), and the material does not tolerate equally high deviatoric stresses before yielding. This means that a material with a small stress ratio, and hence a small friction angle, will dilate or expand easier than with a larger friction angle and stress ratio. The hardening (compaction) is less affected by the change in yield surface.

However, as is seen from figure 6.6 for ridge 3002, increasing M only increases the value of the reaction force. Although the decrease of stress ratio alters the yield surface, the elastic area does not decrease greatly and only for deviatoric stresses.

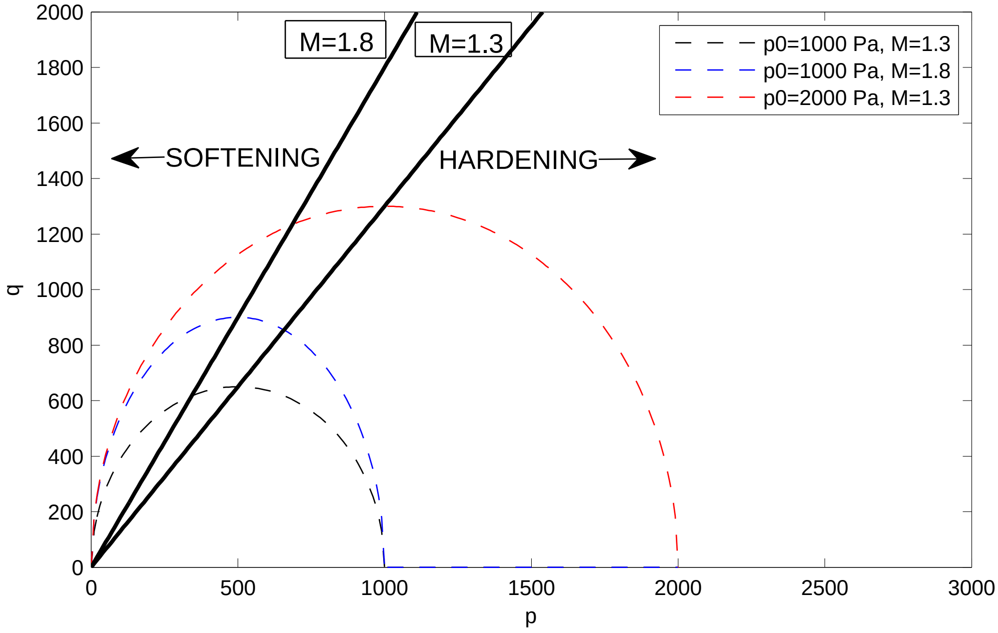

Figure 7.1: *Illustration of the change in yield surface for a change in initial pressure or stress ratio*

Comparing the numerical results with the experimental results, the simulation run with p_0=500 Pa gives a better shape resemblance than the others. The hardening that occurs before maximum force is achieved for this simulation, whereas the simulations run with 2000 and 3000 Pa of initial pressure experiences basically no hardening. For the latter, however, a rather large softening occurs just before the plate is lifted. As is seen in figure 7.1, the change in initial pressure mainly affects the hardening of the material. The increase in initial pressure increases the general stress state in the material, and since the softening is not as much affected by the change in yield surface size, the material softens easier due to higher stresses. The softening effect is not seen in the experimental results. As was mentioned earlier, the ice rubble fails in shear in the first load step of the experiments, and the softening and hardening of the material in the numerical simulations only relates to the changes in volume. The material in other words expands in stead of failing in shear.

Heinonen and Høyland (2013) used a similar model as the Modified Cam Clay model in their simulations of scale-model ridge keel punch tests, but this material model included cohesion. Figure 7.2 shows the shear-cap yield surface. The hardening curve used in this material model is only dependent on the initial pressure, the hardening parameter κ and the initial plastic volumetric strain. The parameter λ is used separately to describe cohesive and frictional softening. Oedometer tests were also simulated in order to *calculate* the cap hardening parameters p_0 and κ, which were estimated to be 368 Pa and 0.08, respectively. Since cohesion is not included in the Modified cam clay model, the parameters cannot be compared directly. Heinonen and Høyland (2013) did a parameter study, using different combinations of Drücker-Prager friction angle and cohesion. The Drücker-Prager friction angle, β, can be related to the stress ratio M and Mohr-Coulomb critical friction angle, ϕ, using compressive matching:

$$M = \tan(\beta) = \frac{6 \cdot \sin(\phi)}{3 - \sin(\phi)}$$

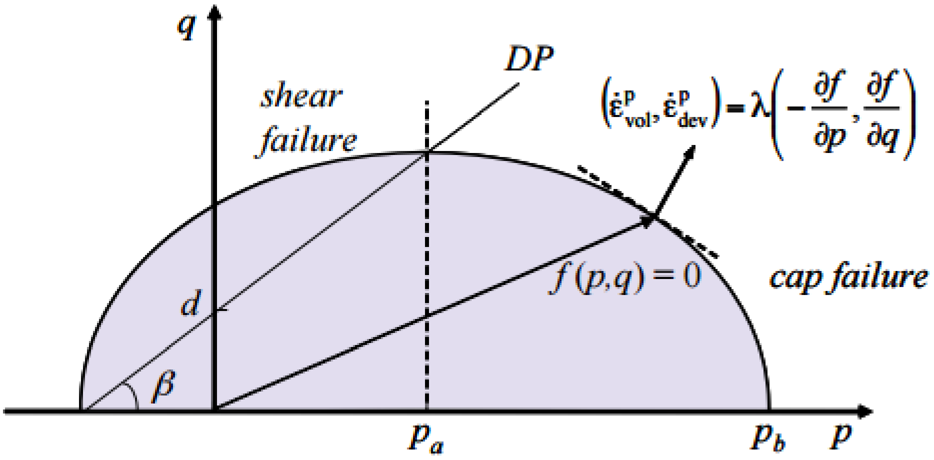

Figure 7.2: *Shear-cap model from Heinonen and Høyland (2013)*

A stress ratio of 1.8 corresponds to a critical friction angle of about 44 degrees, and a Drücker-Prager friction angle of about 60 degrees. β=60 degrees must allegedly be combined with a cohesion of 200 Pa to approach the experimental peak force (Heinonen and Høyland, 2013). If the initial pressure is added with the attraction, which in this case would be $200/\tan(60) = 115Pa$, the yield surface size can be compared to that of this paper. The attraction and initial pressure sums up to almost 500 Pa, which is the same as used for ridge 3002. The effect on the stress state will not be the same seeing as one model accounts for cohesion, and the other one does not. Nevertheless, the initial pressure seems to be in the same order and supports the results from the numerical simulations found in this thesis.

7.1.2 Geometry

The thickness of the consolidated layer is not certain for any of the tests. A smaller thickness gives a uniformly larger force since the depth of ice rubble increases (h_k kept constant, $h_k = h_r + h_{cl}$). Less thickness, however, gives a smaller buoyancy force from the consolidated layer after total submersion, meaning that the difference between the two cases from section 6.1.2 will be less after the time of which the thinnest consolidated layer is submerged.

The keel depth is stated to be 400 mm for ridge 3001 and 700 mm for ridge 3002. For the latter, however, the alleged depth does not correspond to the given cross section for the ridge, which is closer to 400 mm. Neither of the profiles at starboard and port side of the same ridge give a keel depth of that magnitude. A difference in keel depth of 300 mm gives a huge change in keel resistance, which underlines the importance of proper measurements and reporting.

It is evident from the cross sections that the ice rubble does not have a constant depth. In fact the cross sections are more similar to the ideal shape of figure 2.1, at least in the case of ridge 3001, profile 2 (figure 3.4). If a more advanced and geometrically similar model was made, as was done by Liferov et al. (2003) in the finite element software Plaxis, there would be a larger accumulation of ice rubble directly beneath the plate. This, in turn, should give a larger buoyancy and more resistance from the rubble.

A four meter width/length of the ridge has been used in the model. This corresponds to the four meter wide cross sections illustrated previously. The difference is that in the ice tank the ridge is elongated by level ice, and not directly confined by the tank walls at these points. The ice rubble is free to move beyond the width of the ridge. In the numerical model, velocity type boundary conditions restrict the rubble to move outside the vertical boundaries of the domain. For high initial pressure and/or a large stress ratio, the great compaction of the ice causes more material movement in the horizontal direction. Due to the boundary conditions, the material is forced to move back and forth, resulting in oscillations in the plot for the reaction force. This was seen in the results for some of the full scale simulations.

Another way of modelling could be to create a larger domain and letting the consolidated layer/level ice extend beyond the ice rubble, creating a more realistic picture with the tank walls further away from the ridge. This is, however, not an issue for lower values of initial pressure and stress ratio, where there is no material movement near the boundaries. It is hence a larger issue for the full scale simulations.

7.2 Full Scale Simulations

The numerical simulations managed to reach the same value of the peak force as in the experiments. The only exception is test 6, for which it required an unrealistically high initial pressure to approach the experimental value. Heinonen (2004) states that the shear stress for test 6 is so high that they most likely did not manage to cut through the entire consolidated layer during the punch testing. This will explain why the reaction force is so much higher in the experimental results, as the resistance of the consolidated layer will contribute.

The maximum force also appears at the same time for numerical and experimental results, although with a different initial stiffness and with the stiffness changing for the numerical results. The material model seems to be suitable for maximum load calculations of ice ridges.

7.2.1 Load Drops and Applied External Loading

It appears as if the Modified Cam Clay model is not able to capture the material collapse and large softening of the ice rubble. In the experimental results, the reaction force reduces to zero at the end of the tests and has a quite rapid reduction after the first peak. In the numerical results, the difference between the peak force and the residual force is much less and the reaction force is nowhere near reaching zero for the given time interval. The most important reason for this is that failure is not included in the material model. Collapse of the ice rubble skeleton is not possible in the numerical model and it is therefore impossible to simulate the large load-drop after the first peak.

The individual drops of the plate in the full scale tests (probably due to failure of individual ice blocks) has not been taken into account in the simulations. To *simulate* the load drops, one would need to define the changes in displacement or velocity, and Abaqus does not handle prescribed, rapid changes in velocity or displacement well, often giving numerical errors. This is illustrated by the large, sudden load drop in the numerical results of test 10, figure 6.15a, when the velocity is reduced to zero over a short time interval. Rapid changes in velocity or displacement may induce unnatural peaks or stiffness changes. Applying an external load as a forced displacement similar to the measured displacement may yield unnatural results that are more dependent on the prescribed displacement than on the material model. As the material in finite element calculations is reckoned as a continuum mass, one will not retrieve the effect of breakage of individual ice blocks, complicating the simulation of the oscillations after the initial peak. As was mentioned by Heinonen (2004), these oscillations might partly be due to the large amount of strain energy stored in the steel wires. Including the steel wires in the model might help improving the post peak results.

It was shown that the initial stiffness is dependent upon the loading rate. The initial stiffness for test 6 was the only one displaying a *lower* value for the numerical simulation than for the field measurements, and this particular test also had a lower initial plate velocity than the rest of the tests. The stiffer behaviour in the experimental results for this test is, however, more likely because of the contribution from the consolidated layer. The velocities has been calculated from two intervals, the first one ranging to the time of the peak force. A closer look at the displacement plots from the field measurements show that the velocity is actually quite smaller in the very beginning of the test. The use of a lower velocity in the simulations may yield a more similar stiffness to the field measurements, although a somewhat higher stiffness is expected when using finite element calculations due to the unnatural mathematical displacements enforced by the interpolation functions. The comparison of different loading velocities, figure 6.10, enhances the importance of interpreting the loading conditions properly.

7.2.2 Numerical Parameters

The high initial pressure gives a large initial confinement of the ice rubble. For the full scale simulations, the parameter study was mainly about maximizing the reaction force as much as possible. To retrieve the large load capacity of the experimental results, a large initial pressure was necessary. The large confinement makes the ice rubble stiffer and affects the deformation. For small values of initial pressure, the main material movement is directly beneath the platen, whereas for a larger initial pressure the region of material movement expands towards the boundaries, creating a more beam-like bending of the ice rubble volume. For test 10, which has a small rubble depth, even the topmost parts of the ice rubble is moved downwards with the platen. The large initial pressure on such a relatively small rubble depth causes a stiffer material and is most likely the reason for the plastic strains being lower for this test than the others. The volumetric plastic strains are in the order of the other tests, meaning that the plastic shears strains are much lower for test 10. When the deformation is so well distributed through the keel volume, there will be less shear stresses than for the plug deformation. For test 6, almost the entire volume of ice rubble deform, enhancing the theory of a too shallow cut. The large initial pressure, along with a domain length that may have been too small, results in material movement at the boundaries for some of the tests and an oscillating reaction force.

Heinonen (2004) did numerical simulations on full scale punch tests - mainly the ones executed in 2000, but also a couple of the 1999-experiments. These simulations were based on the same material model as in figure 7.2. He, as well, observed that the maximum force increased as the friction angle increased. Another observation was that for a low friction angle, the keel collapses more sharply, the shear failure is more likely and therefore the compaction plays a minor role. He also states that the volumetric expansion is low for a small friction angle. For high friction angles, he states that the material does not really soften because the compaction plays a bigger part. During cap failure, the material hardens in stead of softens. It is, however, not entirely accurate to compare the hardening and softening phenomenon to the current simulations seeing as both a cohesional softening and a failure criterion was included in the simulations of Heinonen (2004).

What, on the other hand *can* be drawn from his conclusions is that for low friction angles, the deviatoric part of the plastic strain describes most of the deformations, and that for high friction angles the material expands only very slightly. The softening that occurred in his simulations for low friction angles was due to cohesional softening, which is not included in the present material model. This would explain why the softening is not any more prominent for low friction angles (low stress ratio M) using the Modified Cam Clay model.

When the stress state approaches the top of the yield surface, the gradient is such that the deviatoric plastic strain will be much higher than the volumetric plastic strain (figure 2.8). The expansion or compaction is thereby limited, and the deviatoric strain will not provide any failure using the Modified

Cam Clay model. When the deviatoric part of the plastic strain describes the deformation, the material will continue shearing without any change in stress or volume. The insignificant decrease in reaction force after the maximum load in the current simulations must be explained by a larger amount of deviatoric plastic strains than that of volumetric plastic strains, and means that the stress state lies near the flat part of the yield surface.

Heinonen (2004) assumed that the ratio of initial pressure to cohesion was the same in model scale and full scale, and based his calculations on a ratio of p_0/d_0=8.55. With a cohesion ranging from 5-25 kPa, this gives an initial pressure ranging from 43 to 214 kPa, which is much higher than the initial pressure in this thesis. Since he concludes that the Drücker-Prager friction angle should be less than 35 degrees, and according to keel deformations, between 15 and 25 degrees, this does not have to indicate that either methods give bad results. A Drücker-Prager friction angle of less than 35 degrees means that the stress ratio M for the Modified cam clay model would have to be less than 0.9. That is a large reduction from the value of 1.85 used in this thesis. Seeing as the stress ratio and the initial pressure did the same trick on the reaction force, the initial pressure would have to be increased extensively to reach the same force for such a smaller M. A doubling of the stress ratio from 0.9 to 1.85 should not be too different from a doubling of the initial pressure, meaning that it is not unlikely that the initial pressure would have reached a value of more than 40 kPa for such a small M. Experiments with different boundary conditions, provoking yield elsewhere on the yield surface, may be required to define M and p_0 better.

7.2.3 Measured Parameters

For a higher porosity, the softening is less. A larger porosity gives a larger material volume and less possibility for the volume to expand. This can be verified by equations (5.1) through (5.3), saying that a larger volume increases the pressure, giving less volumetric strains than for the same pressure on a smaller volume.

The density of solid sea ice is the same for all full scale tests. In reality, the ice density was measured on different sites and at different points, and then given as an average density. It does, however, seem like the density has limited effect on the results.

The cut depth is not necessarily the same as the depth of the consolidated layer. The cut depth may be smaller, in which case the measured reaction force also will contain a contribution from the resistance of the consolidated layer. This may have been the case for full scale test 6. There is also a possibility that individual blocks in the upper parts of the ice rubble could have been partially frozen into the consolidated layer, which also would affect the load resistance. In the numerical model, all contributions from the consolidated layer is excluded, except for the frictional contact between the ice rubble and the consolidated layer. The cut depth may also have been larger than the consolidated layer, in which case the rubble depth was actually larger in reality than what is calculated in this thesis. A larger rubble depth would cause the simulated reaction force to be higher.

7.3 Comparison of Model Scale and Full Scale Simulations

The initial pressure was found to range between 0.5-1 kPa for model scale tests, and 19-24 kPa for full scale tests. This represents a full scale to model scale ratio (p_0^{FS}/p_0^{MS}) of around 20-40. With a keel depth of about 0.4-0.5 m for model scale and 4-5 m for full scale, the length scaling is in the order of 10. The plate diameter, on the other hand, is about 5 times larger for full scale. The initial pressure is in other words not scaled in the same way as the geometry, and shows that the model scale ice ridges are much weaker. Since the ice ridges are made of different materials, one should expect a different scaling of the strength than of the other quantities. The model scale ice ridges are made artificially, and both the microstructure and the temperature development differs. The model scale ice ridges are hence expected to display a softer behaviour.

In the numerical model, the length/width of the ridge was scaled from model scale to full scale in the same manner as the plate diameter, i.e. with a scale factor of 5.5. It would have been more precise to scale the length in the same way as the keel depth, so that the full scale ridges were 10 times longer and wider than the model scale ridges. This might have solved the problem with material movement at the boundaries.

Heinonen and Høyland (2013) compared their results from model scale ridges with the full scale simulations of Heinonen (2004) and came up with a cohesion ratio (d^{FS}/d^{MS}) of 10-25 for Drücker-Prager friction angles between 35 and 45 degrees. The length scaling was about 10 (keel depth and block size). Since the calculations of Heinonen (2004) was based on the assumption that the ratio of initial pressure to cohesion (p_0/d_0) was the same in model scale and full scale, this means that in his model the initial pressure was scaled by the same factor as the cohesion. It is evident that the scaling is not the same for the two different material models, even though the model scale simulations have been performed on two different model scale experiments.

The stress ratio is estimated to be 1.8 for model scale and 1.85 for full scale ice ridges, i.e differing by a value of 0.05. Since the stress ratio is dimensionless and based upon the critical friction angle, it should theoretically be the same for model scale and full scale ice ridges. Since the initial pressure for full scale simulations has the same effect on the results as the stress ratio, the stress ratio could have been kept the same as in model scale by increasing the initial pressure. Such a small decrease in stress ratio would have required an increase in initial pressure of about 0.5 kPa, in which case the values for full scale simulations would have ranged from 19.5-24.5 kPa. The scale factor of 20-40 is not influenced by this.

Figures 7.3 and 7.4 show how the initial pressure relates to the porosity of the ice ridge and the effective rubble depth. The lowest points originate from the model scale ridges. A trend of increasing initial pressure for both increasing porosity and increasing rubble depth is seen, with the rubble depth being the most influential. Test 9, which has the largest effective rubble depth, does not have the highest initial pressure, but it also has a lower porosity (31 %) than the others. In figure 7.3, the highest initial pressure originates from test 2. It does not have the highest porosity, but has a quite larger rubble depth than test 10, which has the largest porosity. The individual material parameters can be viewed in table 7.1.

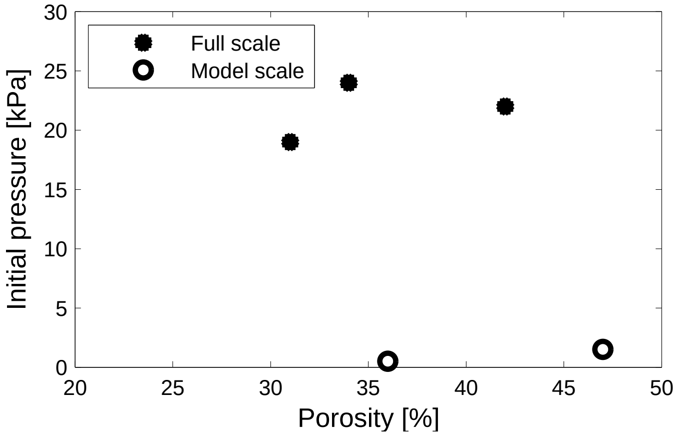

Figure 7.3: *Ice ridge porosity compared with initial pressure*

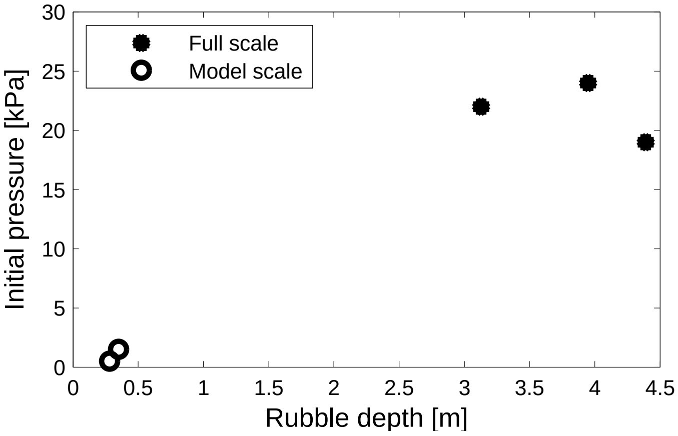

Figure 7.4: *Ice rubble depth compared with initial pressure*

The value of $(\lambda - \kappa)$ is larger for model scale simulations than for the full scale simulations. This is because $(\lambda - \kappa)$ controls the gradient of the hardening curve, and the pressure increases too fast if a small difference is used in the model scale simulations. It does not alter the maximum value of the reaction force in any significant way, but it causes oscillations in the reaction force that may either be due to numerical errors caused by large deformation speed or the phenomenon described earlier - that the material movement reaches the boundaries. For the full scale simulations the main goal was to increase the reaction force as much as possible and the hardening parameter difference was therefore minimized. The hardening parameters has in both cases little significance.

Both maximum principle plastic strains and plastic volumetric strains are smaller for full scale simulations. The maximum principle plastic strains in model scale simulations are about 2 times larger than for full scale simulations. This is caused by the deformation mode, since the maximum principle plastic strain for the two cases is taken from the area of largest strains in figures 6.2a and 6.9a. For model scale, the plastic strains are more concentrated due to the plug deformation, whereas the high initial pressure in full scale simulations causes more well distributed strains and stresses. Total volumetric plastic strains are 3-6 times larger for model scale, meaning that the volumetric expansion plays a bigger role in the deformation for the model scale ridges. In model scale the blocks break easier, and this may be the reason for higher ε_p^p and ε_q^p. Table 7.1 gives a summary of the calculated volumetric strains and corresponding material parameters for all the tests.

Test	ε_p^p [%]	η [%]	h_r [m]	p_0 [kPa]	$(\lambda - \kappa)$
2	0.57	34	3.95	24	0.04
9	0.27	31	4.39	19	0.04
10	0.51	42	3.13	22	0.05
3001CL	1.9	47	0.35	1	0.14
3002CL	1.7	36	0.28	0.5	0.1

Table 7.1: *Volumetric plastic strains and corresponding material parameters*

Even though the hardening parameters did not have a visible effect on the reaction force, they obviously have an effect on the volumetric strains. Such a low difference in hardening parameters as for the full scale simulation gives a large gradient in the hardening curve. This means that large pressures are needed to gain a certain volumetric strain. As has been discussed, the stress state most likely lies on the flat part of the yield surface, causing the deformation to be highly determined by the deviatoric strains. The parameter study on full scale ridges showed that the residual force depended mainly on the initial pressure, and the use of the same hardening parameters as for model scale simulations did not affect the softening in any significant way. This is not so strange seeing as the volumetric strains in either cases are relatively small compared to the deviatoric strains. It is, however, seen that for both model scale and full scale, the simulations with the highest initial pressure provides the largest volumetric plastic strains. As was discussed earlier for model scale simulations, an increase in the yield surface size does not decrease the softening area as much as the hardening area. Since the larger initial pressure increases the general stress state, it will be easier to soften. Table 7.1 contradicts the earlier conclusion on less softening for larger porosity, seeing as the ridges with the highest porosity also displays the largest volumetric expansion. The initial pressure is in other words more important for the softening phenomenon than the porosity.

8 Conclusions

The following conclusions can be drawn from the initial studies:

- Stiffness based hourglass control is preferable for such low-speed dynamic simulations as punch tests on ice.
- The solution is highly mesh dependent. The best results are gained with a grid of regular elements, but with a more dense mesh in the area of material deformation. Irregular elements give bad results.
- Reducing the penalty stiffness improved the accuracy of the results, implying that the software overestimates the penalty stiffness, resulting in numerical error and too much penalty work. This might be due to the weak nature of the material and low stresses.
- When a Lagrangian structure interacts directly with a Eulerian material, sharp edges needs to be avoided.

Additional recommendations for Coupled Eulerian-Lagrangian analyses are included in appendix B.

The Modified cam clay material model successfully managed to fit the experimental results until maximum force. Since the material model does not include a failure criterion, the post-peak region of the full scale reaction force was not possible to imitate. Of the same reason, the second load step in the model scale tests could not be simulated. The model scale ice ridges experienced high plastic strains and remained in the deformed shape when the plate was lifted. Even though the failure of the keel was not simulated, the shear forces developed through the keel in the same area as failure is expected. The plastic volumetric strains, which were in the order of 0.5-2 %, where larger for the model scale than the full scale ice ridges.

A parameter study on full scale and model scale punch tests has been performed. It was shown that the properties with the largest influence on the results, especially the reaction force, was the initial pressure, p_0, and the stress ratio, M. The initial pressure showed a large difference from model scale to full scale ice ridges, with a scale factor of around 20-40. For the model scale ridges, the initial pressure was in the range of 0.5-1 kPa, while for the full scale ridges the same parameter was around 20 kPa. The length scaling was, for comparison, in the order of 10. The scaling is not expected to be the same for the mechanical properties as for the geometrical properties, seeing as the model scale ridges are made artificially and are hence composed of a different material.

The parameter study on model scale and full scale punch tests resulted in a stress ratio M of 1.8 and 1.85, respectively. This corresponds to Mohr-Coulomb friction angles of about 44 and 45 degrees, and is similar to the conclusions of Serré (2011) from his pile tests. The stress ratio is dimensionless and should theoretically be the same for the two cases. However, since the initial pressure and the stress ratio influenced the reaction force in the same manner for full scale simulations, the stress ratio could have remained equal to 1.8 in full scale by increasing the initial pressure by about 0.5 kN. This would not have influenced the estimated scale factor.

The difference between the hardening parameters, $(\lambda - \kappa)$, turned out to have little influence on the resulting reaction force from the simulations. It does, however, seem to affect the volumetric strains. A small difference between λ and κ gives a large gradient in the hardening curve, resulting in high stresses for low plastic volumetric strains. This is possibly the reason for the larger volumetric strains for the model scale ridges than the full scale ridges. The individual value of the hardening parameters has no significance in this material model.

The rubble depth turned out to have a large impact on the resistance of the rubble. Not only does it seem like the assumption of a constant depth for model scale ridges is inaccurate, but it seems like the depth measurements (both in terms of keel and consolidated layer) are vital to obtain good estimations of the material parameters. For the full scale simulations, the consolidated layer thickness should be measured and reported along with the cut depth, seeing as the cut depth is targeted to reach beneath the consolidated layer and into the rubble. This affects the depth of the ice rubble in the simulations, and consequently the reaction force on the loading plate.

The full scale punch tests were performed using a more complicated system than the model scale ice ridges. For one, the velocity was not kept constant which complicates the numerical simulation. In addition, the flexible system with elastic energy stored in the steel wires may be the reason for the oscillations in the reaction force for the experimental results. A more advanced numerical model is probably necessary to control all of the external factors contributing to the reported reaction force.

The Modified cam clay model is not recommended for further analysis on ice ridges. The experiments show that the ice rubble fails at relatively low stresses, at least in model scale tests, and the Modified cam clay model does not consider failure. The ice ridges reportedly fail in shear during punch tests. The Modified cam clay model provides no restrictions on the deviatoric (shear) strains, but the numerical simulations indicate that the deviatoric strains in fact gives the greatest contribution to the plastic strains. In addition, both Heinonen and Høyland (2013), Heinonen (2004) and Liferov et al. (2003) claim that the strength of the ice rubble is dominated by the cohesion, which is absent in the current material model. CEL proved to be an effective and appropriate tool for these types of simulations. A combination of CEL with a more suitable material model would probably be the best way to simulate ice-structure interaction. However, a great disadvantage with the Euler formulation in Abaqus is that it does not support shear failure. User-defined material models can be applied, but unsupported material behaviour should still not be defined as it will cause unpredictable behaviour.

The final section will provide suggestions for further work within this area.

9 Suggestions for Further Work

- The application of external loading in full scale simulations should be investigated more thoroughly, including the effect of varying the prescribed velocity or displacement on the results
- For the full scale tests, further numerical simulations should assess the possibility of modelling the loading as applied to a spring in order to try and capture the post peak behaviour of the ice rubble
- The elastic properties of ice rubble could be described using the Porous elastic material model available in the Abaqus material library, in which the volumetric elastic strain varies with the logarithm of the equivalent pressure stress. This material model, however, is only valid for small elastic strains. The Porous elastic material model can be used in combination with the Critical state (clay) plasticity model (as in this thesis) or one the two types of Drücker-Prager models.
- Since the rubble depth has such a great influence on the results, the approximation of a constant depth of the ice ridge should be investigated. Numerical models should be compared using both an average, constant keel depth and a varying keel depth more geometrically similar to the experiments. It is for the purpose of comparison important that the two models are made in the same software using the same material model and parameters.

References

Chopra, A. K. (2007), *Dynamics of Structures: Theory and Applications to Earthquake Engineering*, third edn, Pearson Prentice Hall.

Cook, R. D. et al. (2002), *Concepts and applications of finite element analysis*, fourth edn, John Wiley & Sons.

Dassault Systémes (2012*a*), *Abaqus 6.12, Abaqus Analysis User's Manual.*

Dassault Systémes (2012*b*), *Abaqus 6.12, Abaqus/CAE User's Manual.*

Dassault Systémes (n.d.), 'Coupled Eulerian-Lagrangian Modeling Techniques, Lecture 4'.

Heinonen, J. (2004), *Constitutive modeling of ice rubble in first-year ridge keel*, VTT Technical Research Centre of Finland.

Heinonen, J. and Høyland, K. V. (2013), Strength and failure mechanisms in scale-model ridge keel punch through tests - FE-analysis, *in* 'Proceedings of the 22nd International Conference on Port and Ocean Engineering under Arctic Conditions, Espoo, Finland'.

Høyland, K. V. (2002), 'Consolidation of first-year sea ice ridges', *Journal of Geophysical Research: Oceans (1978–2012)* **107**(C6), 15–1.

Høyland, K. V. (2007), 'Morphology and small-scale strength of ridges in the north-western barents sea', *Cold Regions Science and Technology* **48**(3), 169–187.

Høyland, K. V. (2010), Thermal aspects of model basin ridges, *in* '20th IAHR International Symposium on Ice'.

Høyland, K. V. (2015), 'Dimensional Analysis and scale-model testing'. Lecture notes TBA4292.

Jensen, A. et al. (2001*a*), Physical modelling of first-year ice ridges - Part I: Production, consolidation and physical properties, *in* 'Proceedings of the 16th International Conference on Port and Ocean Engineering under Arctic Conditions, POAC', Vol. 1, pp. 1483–1492.

Jensen, A. et al. (2001*b*), Physical modelling of first-year ice ridges - Part II: Mechanical properties, *in* 'Proceedings of the 16th International Conference on Port and Ocean Engineering under Arctic Conditions, POAC', Vol. 1, pp. 1493–1502.

Levanger, H. (2012), Simulating ductile fracture in steel using the finite element method: Comparison of two models for describing local instability due to ductile fracture., Master's thesis, University of Oslo.

Liferov, P. and Bonnemaire, B. (2005), 'Ice rubble behaviour and strength: Part I. Review of testing and interpretation of results', *Cold Regions Science and Technology* **41**(2), 135–151.

Liferov, P. et al. (2003), 3D finite element analysis of laboratory punch tests on ice rubble, *in* 'Proceedings of the 17th International Conferance on Port and Ocean Engineering under Artic Conditions, Trondheim, Norway', Vol. 2, pp. 599–610.

Mathisen, K. M. (2014*a*), 'Lecture 11: Solution methods for contact problems'. Lecture notes TKT4197.

Mathisen, K. M. (2014*b*), 'Lecture 9: Solution of the nonlinear dynamic equilibrium equations'. Lecture notes TKT4197.

Nilsen, H. L. (2014), *Material modelling of the non-consolidated layer in first-year ice ridges using the finite element method*, Norwegian University of Science and Technology.

Qiu, G. et al. (2009), Applications of coupled eulerian-lagrangian method to geotechnical problems with large deformations, *in* 'Proceeding of SIMULIA customer conference', pp. 420–435.

Repetto-Llamazares, A. H. V. (2010), Review on model ice ridges, *in* '20th IAHR International Symposium on Ice'.

Serré, N. (2011), Study of the rubble ice action in scale-model ice ridge impact on seabed structures, PhD thesis, NTNU.

Serré, N. et al. (2013), Rubble Ice Transport on Arctic Offshore Structures (RITAS), Part II: 2D scale-model study of the level ice action, *in* 'Proceedings of the 22nd International Conference on Port and Ocean Engineering under Arctic Conditions, Espoo, Finland'.

Standard Norge (2010), 'ISO 19906:2010 Petroleum and natural gas industries - Arctic offshore structures'.

Ştefancu, A.-I. et al. (2011), *Penalty based algorithms for frictional contact problems*, "Gheorghe Asachi" Technical University of Iasi, Faculty of Civil Engineering and Building Services.

Strub-Klein, L. and Sudom, D. (2012), ‘A comprehensive analysis of the morphology of first-year sea ice ridges’, *Cold Regions Science and Technology* **82**, 94–109.

Sudom, D. and Timco, G. (2013), Knowledge gaps in sea ice ridge properties, *in* ‘Proceedings of the 22nd International Conference on Port and Ocean Engineering under Arctic Conditions, Espoo, Finland’.

Timco, G. and Burden, R. (1997), ‘An analysis of the shapes of sea ice ridges’, *Cold Regions Science and Technology* **25**(1), 65–77.

Wood, D. M. (1990), *Soil behaviour and critical state soil mechanics*, Cambridge university press.

A Energy Analyses

1. The geometry of the Eulerian domain is changed from a curved slice with two symmetry axes, to a cube with only one symmetry axis in order to gain a more regular mesh
2. The mesh at the bottom of the cylinder is refined
3. Changed from displacement boundary condition at symmetry axis to velocity boundary condition
4. Stiffness based hourglass control instead of default (viscous)
5. Reduced number of constraints/boundary conditions
6. Changed the contact surfaces
7. Boundary condition at bottom of Eulerian domain: velocity in y-direction equal to zero
8. Increased thickness of void elements at the top of the Eulerian domain
9. Increased mesh density in the slave-structure (Eulerian)
10. Purely elastic material model
11. Von Mises elastic-perfectly plastic material model with metal properties
12. Von Mises elastic-perfectly plastic material model with ice properties
13. Examine the effect of the hardening parameters on Modified Cam Clay: Hardening parameters as is normal for clay
14. Introducing a smooth step amplitude in the constant velocity boundary condition
15. Reducing the automatic time increment: scaling factor from 1 to 0.7
16. Variable mesh: Refined mesh in contact zone, coarser mesh in the rest of the domain
17. As 16, but the refined section is increased to reach the bottom of the Eulerian domain
18. Increase of initial pressure p_0 to 10 kPa
19. Increase of initial pressure p_0 to 100 kPa
20. Increased penalty stiffness: scaling factor $= 0.5$

21. Defining pure master-slave surface weighting (instead of balanced)
22. Introducing contact damping in the friction interaction property: Damping coefficient = 0.5
23. As 22, damping coefficient = 0.8
24. Reduced penalty stiffness: scaling factor = 0.5
25. Reduced penalty stiffness: scaling factor = 0.1
26. Reduced penalty stiffness: scaling factor = 0.01
27. Reduced penalty stiffness: scaling factor = 0.05
28. Reduced penalty stiffness: scaling factor = 0.025
29. The sharp corner at the cylinder bottom is rounded off (r=0.05)

B CEL and Interaction Modelling

B.1 Loads and Boundary Conditions

The material in the Eulerian domain is defined by assigning an initial material location. Default for Eulerian analyses is that the material is allowed to flow in and out of the domain. This means that if there is material in the boundary elements of the Eulerian domain, inflow of material may occur if otherwise is not defined. When material is pushed towards another boundary of the domain, outflow may occur if otherwise is not defined. This will alter both mass and energy in the system.

The inflow can be changed by assigning a *void* inflow or none inflow. For outflow the possibilities include zero pressure outflow, non-reflecting outflow and non-uniform pressure outflow. The "free" inflow and outflow option is the default, allowing both inflow and outflow at the boundaries. The boundary conditions (example for void inflow and nonreflecting outflow) are defined by the command:

```
*EULERIAN BOUNDARY, INFLOW=VOID,
   OUTFLOW=NONREFLECTING
```

The inflow and outflow may also be modified by controlling the velocity at the mesh boundaries, as was done in this thesis.

Remember that the mesh in Eulerian analyses is fixed, while the material is allowed to flow through the elements. This means that boundary conditions and loads that are assigned to a surface or a region of the Eulerian mesh only affects the material when it flows through the specified region or surface. The loads and boundary conditions have no effect when the elements are empty. Since the nodes are fixed, non-zero displacement boundary conditions cannot be used.

B.2 Modelling Recommendations

- The best accuracy is achieved using regular elements in the Eulerian mesh. For the simulation to manage tracking the material boundaries, the mesh should be particularly dense in the region where material movement is expected.
- When using two Eulerian materials in the same domain, the contact is defined as sticky, and relative motion between two materials in the

same element is not allowed. If a more complex contact definition is required, one of the materials needs to be of a Lagrangian formulation, for which a general contact definition is available.

- If the Lagrangian structure lies outside the Eulerian mesh there needs to be a gap between the structure and the Eulerian material for which contact is defined.
- If the Lagrangian structure is *inside* the Eulerian mesh one must make sure that there is only void in the underlying Eulerian elements. Two materials can never occupy the same space.
- Contact is only enforced when the material volume fraction in the element is greater than 0.5. Hence, you may experience some penetration of material into the Lagrangian domain. This effect can be reduced by refining the Eulerian mesh in the area, or by rounding sharp edges/corners in the contact surface of the Lagrangian structure. The edges may be rounded using a fillet with radius equal to the size of the nearest Eulerian elements.
- When defining Eulerian-Lagrangian contact, one cannot use Lagrangian beam, truss or pipe elements, or analytical rigid surfaces.
- Some material definitions are unsupported in the Eulerian formulation, such as shear failure and anisotropy. User-defined material models should therefore be used with caution.

B.3 Output

For Eulerian elements, volume averaged output must be selected. Output for stress is for example given as SVAVG - volume averaged stress. The parameter EVF, Eulerian volume fraction, needs to be requested in order to view the material location in the visualization mode. Be aware that the field output requests, such as EVF, produce large output files, especially for a fine mesh.

The total mass of the material should be monitored to warn of undesired material loss. This is attained by requesting an integrated output for the mass. Integrated output can only be requested using the keyword editor or by changing the input file (not available in GUI). If the total volume or volume change is of interest, this must also be selected as an integrated output, using the variable VOLEUL. The keywords for the input file are given below.

```
**
**HISTORY OUTPUT
**
*Output, history, variable=PRESELECT
    *INTEGRATED OUTPUT, ELSET="name of element set"
        MASSEUL
**
**HISTORY OUTPUT
**
*Output, history, variable=PRESELECT
    *INTEGRATED OUTPUT, ELSET="name of element set"
        VOLEUL
```

C Conversion Table for Friction Angles

Equation (C.1)-(C.3) gives the compressive, tensile and shear/plane strain matching between the Mohr-Coulomb (ϕ), and the Drücker-Prager friction angle (β). In table C.1 the corresponding values for β is given for a ϕ ranging from 5-50 degrees.

Compressive matching:

$$\tan(\beta) = \frac{6 \cdot \sin(\phi)}{3 - \sin(\phi)} \tag{C.1}$$

Tensile matching:

$$\tan(\beta) = \frac{6 \cdot \sin(\phi)}{3 + \sin(\phi)} \tag{C.2}$$

Shear/plane strain matching:

$$\tan(\beta) = \sqrt{3} \cdot \sin(\phi) \tag{C.3}$$

Mohr-Coulomb	Drücker-Prager friction angle, β		
friction angle, ϕ	Compressive	Tensile	Shear/plane strain
5	10	10	9
10	20	18	17
15	30	25	24
20	38	32	31
25	45	37	36
30	50	41	41
35	55	44	45
40	59	47	48
45	62	49	51
50	64	51	53

Table C.1: *Drücker-Prager friction angle, β, for different values of Mohr-Coulomb friction angles, ϕ*